

Final spins from the merger of precessing binary black holes

Michael Kesden* and Ulrich Sperhake†

California Institute of Technology, MC 350-17, 1216 E. California Blvd., Pasadena, CA 91125

Emanuele Berti‡

*Department of Physics and Astronomy, The University of Mississippi, University, MS 38677-1848, USA and
California Institute of Technology, MC 350-17, 1216 E. California Blvd., Pasadena, CA 91125*

(Dated: February 2010)

The inspiral of binary black holes is governed by gravitational radiation reaction at binary separations $r \lesssim 1000M$, yet it is too computationally expensive to begin numerical-relativity simulations with initial separations $r \gtrsim 10M$. Fortunately, binary evolution between these separations is well described by post-Newtonian equations of motion. We examine how this post-Newtonian evolution affects the distribution of spin orientations at separations $r \simeq 10M$ where numerical-relativity simulations typically begin. Although isotropic spin distributions at $r \simeq 1000M$ remain isotropic at $r \simeq 10M$, distributions that are initially partially aligned with the orbital angular momentum can be significantly distorted during the post-Newtonian inspiral. Spin precession tends to align (anti-align) the binary black hole spins with each other if the spin of the more massive black hole is initially partially aligned (anti-aligned) with the orbital angular momentum, thus increasing (decreasing) the average final spin. Spin precession is stronger for comparable-mass binaries, and could produce significant spin alignment before merger for both supermassive and stellar-mass black hole binaries. We also point out that precession induces an intrinsic accuracy limitation ($\lesssim 0.03$ in the dimensionless spin magnitude, $\lesssim 20^\circ$ in the direction) in predicting the final spin resulting from the merger of widely separated binaries.

PACS numbers: 04.25.dg, 04.25.Nx, 04.70.-s, 04.30.Tv

I. INTRODUCTION

The existence of black holes is a fundamental prediction of general relativity. Isolated individual black holes are stationary solutions to Einstein's equations, but binary black holes (BBHs) can inspiral and eventually merge. BBH mergers offer a unique opportunity to test general relativity in the strong-field limit, and as such are a primary science target for current and future gravitational-wave (GW) observatories like LIGO, VIRGO, LISA, and the Einstein telescope. BBH mergers are also important for cosmology, as they can serve as standard candles to help determine the geometry and hence energy content of the universe [1, 2]. Astrophysical BBHs are found on at least two very different mass scales. Compact objects believed to be stellar-mass black holes have been observed in binary systems with more luminous companions. These black holes are the remnants of massive main-sequence stars, and binary systems with two such stars may ultimately evolve into BBHs. On larger scales, supermassive black holes (SBHs) with masses $10^6 \lesssim M/M_\odot \lesssim 10^9$ reside in the centers of most galaxies. They can be observed through their dynamical influence on surrounding gas and stars, and when accreting as active galactic nuclei (AGN). SBHs will form binaries as well, following the merger of two galaxies which

each host an SBH at their center.

In order to merge, BBHs must find a way to shed their orbital angular momentum. At large separations, binary SBHs will be escorted inwards by dynamical friction between their host galaxies [3]. The BBHs become gravitationally bound when the sum of their masses $M \equiv m_1 + m_2$ exceeds the mass of gas and stars enclosed by their orbit. The binary hardens further by scattering stars on “loss-cone” orbits that pass within a critical radius [4], though this scattering may stall at separations $r \simeq 0.01 - 1$ pc unless these orbits are refilled by stellar diffusion [5]. Unlike stars, gas can cool to form a circumbinary disk about the BBHs. A circumbinary disk of mass M_d and radius r_d will exert a tidal torque

$$T_d \sim \frac{q^2 M_d M}{r} \left(\frac{r}{r_d - r} \right)^3 \quad (1.1)$$

on the binary in the limit that the BBH mass ratio $q \equiv m_2/m_1 \leq 1$ is small and $|r_d - r| \ll r$ [6–8]. Throughout this paper we use relativists' units in which Newton's constant G and the speed of light c are unity. At a sufficiently small separation r_{GW} , the magnitude of this tidal torque will fall below that of the radiation-reaction torque [9]

$$T_{\text{GW}} = \frac{32\eta^2 M^{9/2}}{5r^{7/2}}, \quad (1.2)$$

where $\eta \equiv m_1 m_2 / M^2$ is the symmetric mass ratio. Once $T_{\text{GW}} > T_d$, the inspiral of the BBH is dominated by radiation reaction. The precise value of r_{GW} depends on

*Electronic address: kesden@tapir.caltech.edu

†Electronic address: sperhake@tapir.caltech.edu

‡Electronic address: berti@phy.olemiss.edu

the properties of the circumbinary disk, but an order-of-magnitude estimate is given by [3]

$$r_{\text{GW}} = (5 \times 10^{16} \text{ cm}) q^{1/4} M_8^{3/4} \left[\frac{\min(t_h, t_{\text{gas}})}{10^8 \text{ yr}} \right]^{1/4} \quad (1.3a)$$

$$= (3000M) \left(\frac{q}{M_8} \right)^{1/4} \left[\frac{\min(t_h, t_{\text{gas}})}{10^8 \text{ yr}} \right]^{1/4} \quad (1.3b)$$

where M_8 is the mass of the larger black hole in units of $10^8 M_\odot$, t_h is the dynamical friction timescale for a hard binary, and t_{gas} is the evolution timescale from gaseous tidal torques.

General relativity completely determines the inspiral of BBH systems from separations less than r_{GW} . These systems are fully specified by 7 parameters: the mass ratio q and the 3 components of each dimensionless spin $\chi_{1,2} \equiv \mathbf{S}_{1,2}/m_{1,2}^2$. To a good approximation the individual masses and spin magnitudes $\chi_{1,2} \equiv |\chi_{1,2}|$ remain constant during the inspiral, so only the precession of the two spin directions needs to be calculated. At an initial separation $r_i = 1000M \sim r_{\text{GW}}$, the binary's orbital speed $v/c \ll 1$ and the spin-precession equations can therefore be expanded in this small post-Newtonian (PN) parameter. The PN expansion remains valid until the BBHs reach a final separation $r_f = 10M$, after which their evolution can only be described by fully nonlinear numerical relativity (for more precise assessments of the validity of the PN expansion for spinning precessing binaries, see e.g. [10, 11]). Numerical relativists can simulate BBH mergers from separations $r_{\text{NR}} \simeq r_f$ [12–14], but these simulations are too computationally expensive to begin when the binaries are much more widely separated. The GWs produced in the merger and the mass, spin, and recoil velocity of the final black hole depend sensitively on the orientation of the BBH spins at r_{NR} , so it is important to determine what BBH spin orientations are expected at r_i and whether these orientations are modified by the PN evolution between r_i and r_f .

The answer to the first of these questions comes from astrophysics, not general relativity. At very large separations, the two black holes are unaffected by each other and one would therefore expect an isotropic distribution of spin directions. However, an isotropic distribution of spins at r_f would imply that most mergers would result in a gravitational recoil of $\sim 1000 \text{ km/s}$ for the final black hole [15–17]. Recoils this large would eject SBHs from all but the most massive host galaxies [18], in seeming contradiction to the observed tight correlations between SBHs and their hosts [19–21]. This problem can be avoided if Lense-Thirring precession and viscous torques align the spins of the BBHs with the accretion disk responsible for their inwards migration [22–24]. The efficiency of this alignment depends on the properties of the accretion disk, but N -body simulations using smoothed-particle hydrodynamics (SPH) suggest that the residual misalignment of the BBH spins with their accretion disk at r_i could typically be $\sim 10^\circ$ (30°) for cold (hot) accretion disks [17].

The second question, does the distribution of spin directions change as the BBHs inspiral from r_i to r_f , can be answered by evolving this distribution over this interval using the PN spin-precession equations. We will describe these PN equations and our numerical solutions to them in Sec. II. The precession of a given spin configuration in the PN regime can be understood in terms of the proximity of that configuration to the nearest spin-orbit resonance. Schnittman [25] identified a set of equilibrium spin configurations in which both black hole spins and the orbital angular momentum lie in a plane, along with the total angular momentum $\mathbf{J} = \mathbf{L} + m_1^2 \chi_1 + m_2^2 \chi_2$. In the absence of radiation reaction, \mathbf{J} is conserved. For these equilibrium configurations, the spins and orbital angular momentum remain coplanar and precess jointly about \mathbf{J} with the angles $\theta_{1,2}$ between \mathbf{L} and $\chi_{1,2}$ remaining fixed. The equilibrium configurations can thus be understood as spin-orbit resonances since the precession frequencies of \mathbf{L} and $\chi_{1,2}$ about \mathbf{J} are all the same. Once radiation reaction is added, the spins and orbital angular momentum remain coplanar as the BBHs inspiral, although θ_1 and θ_2 slowly change on the inspiral timescale. Not only do resonant configurations remain resonant, but configurations near resonance can be captured into resonance during the inspiral. The resonances are thus very important for understanding the evolution of generic BBH systems, although the resonances themselves only occupy a small portion of the 7-dimensional parameter space characterizing generic mergers. We shall review these spin-orbit resonances in more detail in Sec. III.

Bogdanović *et al.* [23] briefly considered whether spin-orbit resonances could effectively align SBH spins with the orbital angular momentum following the merger of gas-poor galaxies. They found that for a mass ratio $q = 9/11$ and maximal spins $\chi_1 = \chi_2 = 1$, an isotropic distribution of spins at $r_i = 1000M$ remains isotropically distributed when evolved to $r_f = 10M$. They therefore concluded that an alternative mechanism, such as the accretion torques considered later in their paper, is needed to align the BBH spins with \mathbf{L} . This conclusion is supported by a much larger set of PN inspirals presented by Herrmann *et al.* [26] who found that for equal-mass BBHs, an isotropic distribution of spins at $40M$ yields a flat distribution in $\cos \theta_{12}$ at $7.4M$. Here and in this paper θ_{12} is the angle between the two spins χ_1 and χ_2 . In the final plot of their paper, Herrmann *et al.* [26] revealed their discovery of an anti-correlation between the initial and final values of $\cos \theta_{12}$ for $q = 2/3$ BBHs with equal dimensionless spins $\chi_1 = \chi_2 = 0.05$. Investigation of this anti-correlation was left to future work. Lousto *et al.* [27] also found indications that an initially isotropic distribution of spins can become non-isotropic during the PN stage of the inspiral. For a range of mass ratios $1/16 \leq q \leq 1$ and equal spins $\chi_1 = \chi_2 = (0.485, 0.686, 0.97)$, they found that an isotropic spin distribution at $50M$ develops a slight but statistically significant tendency towards anti-alignment with the orbital angular momentum \mathbf{L} . This amplitude

of anti-alignment scales linearly in the BBH spin magnitudes and appears to decrease as $q \rightarrow 0$.

We perform our own study of PN spin evolution from r_i to r_f for several reasons. BBHs get locked into spin-orbit resonances at a separation

$$r_{\text{lock}} \propto \left(\frac{\chi_1 \cos \theta_1 - q^2 \chi_2 \cos \theta_2}{1 - q^2} \right)^2 M, \quad (1.4)$$

which can become large in the equal-mass ($q \rightarrow 1$) limit [25]. This limit is important, as the largest recoil velocities occur for nearly equal-mass mergers. Numerical integration of the PN equations has shown that for a mass ratio $q = 9/11$, spin-orbit resonances affect spin orientations at separations $r \simeq 1000M$. This is a much larger separation than was considered in previous studies [26, 27] of spin alignment, which may therefore have failed to capture the full magnitude of the effect. These studies also focused on whether an initially isotropic distribution of spins becomes anisotropic just prior to merger. However, as discussed above, tidal torques from a circumbinary disk partially align spins with the orbital angular momentum at separations $r \gg r_{\text{GW}}$ before relativistic effects become important. As we will show in Sec. IV, such partially aligned distributions can be strongly affected by spin-orbit resonances despite the fact that isotropic distributions remain nearly isotropic. We will consider how spin precession affects the final spin magnitudes and directions in Sec. V. The evolution of the distribution of BBH spin directions between r_i and r_f changes the distribution of final spin magnitudes and directions from what it would have been in the absence of precession. In addition, spin precession introduces a fundamental uncertainty in predicting the final spin of a given BBH system. At large separations, a small uncertainty in the separation leads to an uncertainty in the predicted time until merger that exceeds the precession time. In this case, one cannot predict at what phase of the spin precession the merger will occur and thus the resulting final spin. We will explore this uncertainty in Sec. VI. A brief discussion of the chief findings of this paper is given in Sec. VII.

II. POST-NEWTONIAN EVOLUTION

We evolve spinning BBH systems along a sequence of quasi-circular orbits according to the PN equations of motion for precessing binaries first derived by Kidder [28], and later used by Buonanno, Chen and Vallisneri to build matched-filtering template families for GW detection [29]. The adiabatic evolution of the binary's orbital frequency is described including terms up to 3.5PN or-

der, and spin effects are included up to 2PN order. These evolution equations were chosen for consistency with previous work, in particular with the study by Barausse and Rezzolla [30] of the final spin resulting from the coalescence of BBHs and with the statistical investigation of spinning BBH evolutions using Graphics Processing Units by Herrmann *et al.* [26]. Lousto *et al.* [27] evolved a large sample of spinning BBH systems using a non-resummed, PN expanded Hamiltonian. The convergence properties of non-resummed Hamiltonians for spinning BBH systems are somewhat problematic (see e.g. Fig. 1 of Ref. [10]), and it will be interesting to repeat these statistical investigations of precessing BBH systems using the effective-one-body resummations of the PN Hamiltonian recently proposed by Barausse *et al.* [31, 32].

In our simulations, the spins evolve according to

$$\dot{\mathbf{S}}_1 = \bar{\boldsymbol{\Omega}}_1 \times \mathbf{S}_1, \quad (2.1a)$$

$$\dot{\mathbf{S}}_2 = \bar{\boldsymbol{\Omega}}_2 \times \mathbf{S}_2, \quad (2.1b)$$

where

$$\bar{\boldsymbol{\Omega}}_1 = \frac{1}{2r^3} \left[\left(4 + 3q - \frac{3(\mathbf{S}_2 + q\mathbf{S}_1) \cdot \mathbf{L}_N}{L_N^2} \right) \mathbf{L}_N + \mathbf{S}_2 \right], \quad (2.2a)$$

$$\bar{\boldsymbol{\Omega}}_2 = \frac{1}{2r^3} \left[\left(4 + \frac{3}{q} - \frac{3(\mathbf{S}_1 + q^{-1}\mathbf{S}_2) \cdot \mathbf{L}_N}{L_N^2} \right) \mathbf{L}_N + \mathbf{S}_1 \right] \quad (2.2b)$$

are the spin precession frequencies averaged over a circular orbit, including the quadrupole-monopole interaction [33],

$$\mathbf{L}_N = \eta M \mathbf{r} \times \mathbf{v} = \frac{\eta M^2}{(M\omega)^{1/3}} \hat{\mathbf{L}}_N \quad (2.3)$$

is the Newtonian orbital angular momentum, and

$$\omega = \left(\frac{M}{r^3} \right)^{1/2} \quad (2.4)$$

is the orbital frequency. In the absence of gravitational radiation, \mathbf{J} and $|\mathbf{L}_N|$ are constant, implying that the direction of the orbital angular momentum evolves according to

$$\dot{\hat{\mathbf{L}}}_N = -\frac{(M\omega)^{1/3}}{\eta M^2} \frac{d\mathbf{S}}{dt} \quad (2.5)$$

where $\mathbf{S} = \mathbf{S}_1 + \mathbf{S}_2$. Once radiation reaction is included, the orbital frequency slowly evolves as

$$\begin{aligned}
\dot{\omega} = & \omega^2 \frac{96}{5} \eta (M\omega)^{5/3} \left\{ 1 - \frac{743 + 924\eta}{336} (M\omega)^{2/3} + \left[\left(\frac{19}{3}\eta - \frac{113}{12} \right) \boldsymbol{\chi}_s \cdot \hat{\mathbf{L}}_N - \frac{113\delta}{12} \boldsymbol{\chi}_a \cdot \hat{\mathbf{L}}_N + 4\pi \right] (M\omega) \right. \\
& + \left\{ \left(\frac{34103}{18144} + \frac{13661}{2016}\eta + \frac{59}{18}\eta^2 \right) - \frac{\eta\chi_1\chi_2}{48} (247\hat{\mathbf{S}}_1 \cdot \hat{\mathbf{S}}_2 - 721(\hat{\mathbf{L}}_N \cdot \hat{\mathbf{S}}_1)(\hat{\mathbf{L}}_N \cdot \hat{\mathbf{S}}_2)) \right. \\
& + \sum_{i=1}^2 \frac{(m_i\chi_i)^2}{M^2} \left[\frac{5}{2} (3(\hat{\mathbf{L}}_N \cdot \hat{\mathbf{S}}_i)^2 - 1) + \frac{1}{96} (7 - (\hat{\mathbf{L}}_N \cdot \hat{\mathbf{S}}_i)^2) \right] \left. \right\} (M\omega)^{4/3} \\
& - \frac{4159 + 15876\eta}{672} \pi (M\omega)^{5/3} + \left[\left(\frac{16447322263}{139708800} - \frac{1712\gamma_E}{105} + \frac{16\pi^2}{3} \right) + \left(-\frac{273811877}{1088640} + \frac{451\pi^2}{48} - \frac{88}{3}\hat{\theta}\eta \right) \eta \right. \\
& + \left. \frac{541}{896}\eta^2 - \frac{5605}{2592}\eta^3 - \frac{856}{105} \log[16(M\omega)^{2/3}] \right] (M\omega)^2 + \left(-\frac{4415}{4032} + \frac{358675}{6048}\eta + \frac{91495}{1512}\eta^2 \right) \pi (M\omega)^{7/3} \left. \right\}
\end{aligned} \tag{2.6}$$

where $\gamma_E \simeq 0.577$ is Euler's constant, $\hat{\theta} \equiv 1039/4620$, and we have defined

$$\boldsymbol{\chi}_s \equiv \frac{1}{2}(\boldsymbol{\chi}_1 + \boldsymbol{\chi}_2), \tag{2.7a}$$

$$\boldsymbol{\chi}_a \equiv \frac{1}{2}(\boldsymbol{\chi}_1 - \boldsymbol{\chi}_2). \tag{2.7b}$$

The two terms in square parentheses on the third line of Eq. (2.6) are due to the quadrupole-monopole interaction [34] and to the spin-spin self interaction [35], respectively, and they were neglected in the statistical study of Ref. [26]. Their sum agrees with Eq. (5.17) of Ref. [36].

The numerical integration of this system of ordinary differential equations is performed using the adaptive stepsize integrator STEPPERDOPR5 [37]. The evolution of any given BBH system is specified by the following parameters: the initial orbital frequency ω_i , the binary's mass ratio $q \equiv m_2/m_1$, the dimensionless magnitude of each spin χ_i , and the relative orientation (θ_i, ϕ_i) of each spin with respect to the orbital angular momentum at time $t = 0$ ($i = 1, 2$). To monitor the variables along the whole evolution we output all quantities using a constant logarithmic spacing in the orbital frequency at low frequencies, and the stepsize as used in the integrator at high frequencies. Typically this results in a total of about 64,000 points in the range $M\omega \in [M\omega_i, M\omega_f]$, where $M\omega_i = 3.16 \times 10^{-5}$ and $M\omega_f = 0.1$. Numerical experimentation indicates that a tolerance parameter $\text{ATOL} = 2 \times 10^{-8}$ in the adaptive stepsize integrator is sufficient for a pointwise accuracy of order 1% or better in the final quantities. Therefore the error induced by the numerical integrations of the PN equations of motion is subdominant with respect to the errors induced by precessional effects and by fits of the numerical simulations, which will be one of the main topics of this paper.

III. SPIN-ORBIT RESONANCES

In this Section, we review the equilibrium configurations of BBH spins first presented in Schnittman [25] for

which the Newtonian orbital angular momentum \mathbf{L}_N and individual spins $\mathbf{S}_{1,2}$ all precess at the same resonant frequency. As discussed briefly in the Introduction, at a given binary separation r fully general quasi-circular BBHs are described by 7 parameters: the mass ratio q and the 3 components of each black hole spin. In spherical coordinates with \mathbf{L}_N defining the z -axis, each spin is given by its magnitude $S_i = m_i^2 \chi_i$ and direction (θ_i, ϕ_i) ($i = 1, 2$). In the PN limit for which this analysis is valid, a clear hierarchy

$$t_{\text{orb}} \ll t_p \ll t_{\text{GW}} \tag{3.1}$$

exists between the orbital time $t_{\text{orb}} \propto r^{3/2}$, the precession time $t_p \sim \Omega_{1,2}^{-1} \propto r^{5/2}$, and the radiation time $t_{\text{GW}} \sim \dot{E}_{\text{GW}}/E \propto r^4$. This hierarchy implies that the BBH spins will precess many times before merger leaving only their *relative* angular separation $\Delta\phi \equiv \phi_2 - \phi_1$ in the orbital plane well defined. This reduces the BBH parameter space to 6 dimensions. Since the mass ratio and individual spin magnitudes are preserved during the inspiral, a given BBH evolves through the 3-dimensional parameter space $(\theta_1, \theta_2, \Delta\phi)$ on the precession timescale t_p . This evolution is governed by the spin precession equations (2.1).

Schnittman [25] discovered a one-parameter family of equilibrium solutions to these equations for which $(\theta_1, \theta_2, \Delta\phi)$ remain fixed on the precession timescale t_p . These solutions have $\Delta\phi = 0^\circ$ or 180° , implying that \mathbf{L}_N , \mathbf{S}_1 and \mathbf{S}_2 all lie in a plane and precess at the same resonant frequency about the total angular momentum \mathbf{J} , which remains fixed in the absence of gravitational radiation. The values of $\theta_{1,2}$ for these resonances can be determined by requiring the first and second time derivatives of $\mathbf{S}_1 \cdot \mathbf{S}_2$ to vanish. This is equivalent to satisfying the algebraic constraint

$$\begin{aligned}
& (\bar{\boldsymbol{\Omega}}_1 \times \mathbf{S}_1) \cdot [\mathbf{S}_2 \times (\mathbf{L}_N + \mathbf{S}_1)] \\
& = (\bar{\boldsymbol{\Omega}}_2 \times \mathbf{S}_2) \cdot [\mathbf{S}_1 \times (\mathbf{L}_N + \mathbf{S}_2)] .
\end{aligned} \tag{3.2}$$

Since \mathbf{L}_N appears in Eq. (3.2) both explicitly and implicitly through $\bar{\boldsymbol{\Omega}}_{1,2}$, the resonant values of $\theta_{1,2}$ vary with

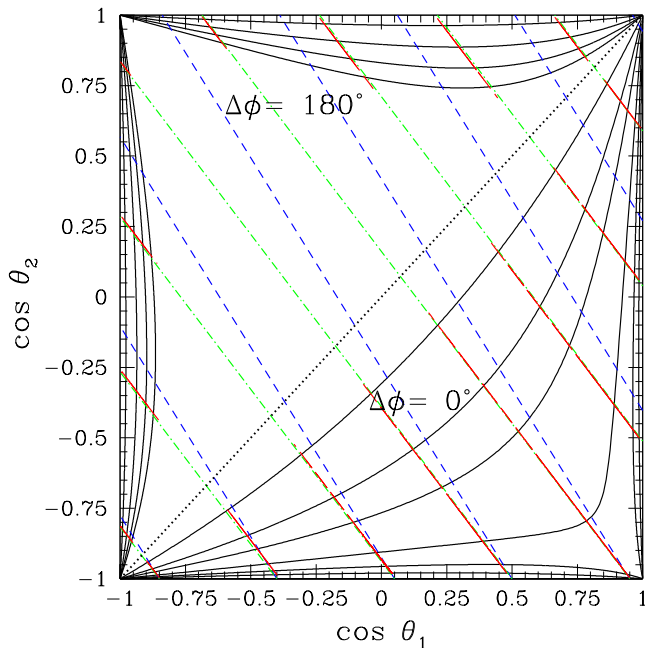


FIG. 1: Spin-orbit resonances for maximally spinning BBHs with a mass ratio of $q = 9/11$. The dotted black diagonal indicates where $\theta_1 = \theta_2$. Solid black curves below (above) this diagonal show (θ_1, θ_2) for the one-parameter families of equilibrium spin configurations with $\Delta\phi = 0^\circ(180^\circ)$ at different fixed binary separations. Approaching the diagonal from below, these curves correspond to separations $r = 1000, 500, 250, 100, 50, 10M$. The curves approaching from above correspond to separations $r = 250, 50, 20, 10M$. The long-dashed red curves show how $\theta_{1,2}$ evolve as members of these resonant families inspiral from $r_i = 1000M$ to $r_f = 10M$. The projection $\mathbf{S} \cdot \hat{\mathbf{L}}_N$ of the total spin \mathbf{S} onto the orbital angular momentum \mathbf{L}_N is constant along the short-dashed blue lines, while the projection $\mathbf{S}_0 \cdot \hat{\mathbf{L}}_N$ of the EOB spin \mathbf{S}_0 is constant along the dot-dashed green lines.

the binary separation. This is crucial, as otherwise these one-parameter families of resonances would affect only a small portion of the 3-dimensional parameter space $(\theta_1, \theta_2, \Delta\phi)$ through which generic BBH configurations evolve. As gravitational radiation slowly extracts angular momentum from the binary on the radiation time t_{GW} , the resonances sweep through a significant portion of the (θ_1, θ_2) plane. The angular separation $\Delta\phi$ of a generic BBH is varying on the much shorter precession time t_p , and thus has a significant chance to closely approach the resonant values $\Delta\phi = 0^\circ$ or 180° at some point during the long inspiral. Such generic BBHs will be strongly influenced or even captured by the spin-orbit resonances, as we will see in detail in Sec. IV.

We show the dependence of the spin-orbit resonances on r for maximally spinning BBHs in Figs. 1 and 2. Those resonances with $\Delta\phi = 0^\circ$ (shown in Fig. 2 of [25]) always have $\theta_1 < \theta_2$, and thus appear below the diagonal

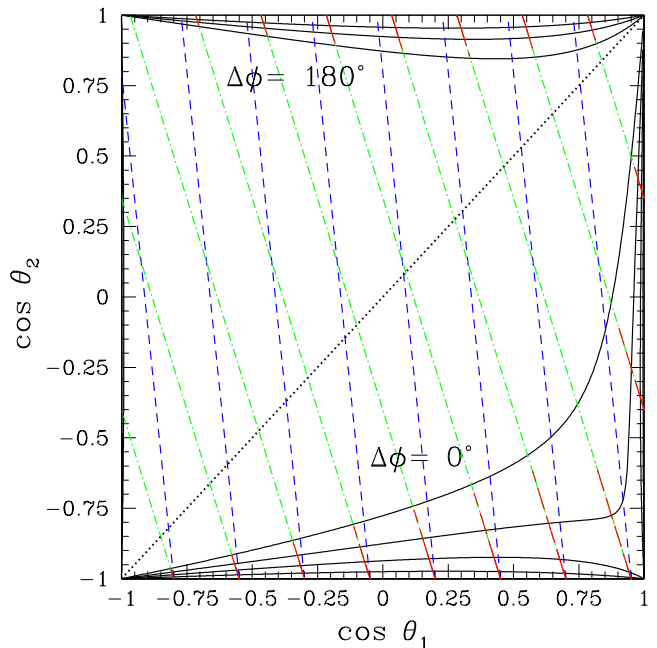


FIG. 2: Spin-orbit resonances for maximally spinning BBHs with a mass ratio of $q = 1/3$. Other than the different mass ratio, this figure is very similar to Fig. 1. The solid black curves approaching the diagonal from below correspond to the families of resonant spin configurations at $r = 50, 20, 10, 5M$, while those approaching from above correspond to separations $r = 20, 10, 5M$.

$\cos\theta_1 = \cos\theta_2$ in our Figs. 1 and 2. Those resonances with $\Delta\phi = 180^\circ$ (shown in Fig. 3 of [25]) have $\theta_1 > \theta_2$ and therefore appear above the diagonal in our Figs. 1 and 2. We plot $(\cos\theta_1, \cos\theta_2)$ rather than (θ_1, θ_2) like [25] because isotropically oriented spins should have a flat distribution in these variables.

In the limit $r \rightarrow \infty$, so that also $|\mathbf{L}_N| \rightarrow \infty$, the resonant configurations either have \mathbf{S}_1 or \mathbf{S}_2 aligned or anti-aligned with \mathbf{L}_N (either θ_1 or θ_2 equals to 0° or 180°). This corresponds to the four edges of the plot in Fig. 1. For smaller fixed values of $|\mathbf{L}_N|$, the values (θ_1, θ_2) for the one-parameter families of resonant configurations approach the diagonal $\theta_1 = \theta_2$. BBHs in spin-orbit resonances at large values of $|\mathbf{L}_N|$ (large r) remain resonant as they inspiral. As gravitational radiation carries away angular momentum, r decreases and $\theta_{1,2}$ for individual resonant BBHs evolves towards this diagonal along the red long-dashed curves in Fig. 1. For resonances with $\Delta\phi = 0^\circ$ (those below the diagonal), this evolution aligns the two spins with each other. Symmetry implies that aligning the spins with each other will lead to larger final spins and smaller recoil velocities [38, 39].

The projection

$$\mathbf{S} \cdot \hat{\mathbf{L}}_N = S_1 \cos\theta_1 + S_2 \cos\theta_2 \quad (3.3)$$

of the total spin $\mathbf{S} \equiv \mathbf{S}_1 + \mathbf{S}_2$ parallel to the orbital an-

gular momentum is constant along the short-dashed blue lines in Figs. 1 and 2. These blue lines have steeper slopes than the red lines along which the resonant binaries inspiral. This implies that the total spin \mathbf{S} becomes anti-aligned (aligned) with the orbital angular momentum for resonant configurations with $\Delta\phi = 0^\circ(180^\circ)$, leading to smaller (larger) final spins. The families of resonances with $\Delta\phi = 0^\circ$ (below the diagonal) sweep through a larger area of the $(\cos\theta_1, \cos\theta_2)$ plane as the BBHs inspiral, and approach the diagonal more closely. This implies that anti-alignment may be more effective than alignment, which might explain the “small but statistically significant bias of the distribution towards counter-alignment” in $\mathbf{S} \cdot \hat{\mathbf{L}}_N$ noted in Lousto *et al.* [27]. However, Table IV of [27] indicates that both \mathbf{S}_1 and \mathbf{S}_2 individually become anti-aligned with $\hat{\mathbf{L}}_N$, whereas the spin-orbit resonances would align one black hole while anti-aligning the other. All of the PN evolutions in Lousto *et al.* [27] begin at separations of $r = 50M$, which corresponds to the $\Delta\phi = 0^\circ$ curve in Fig. 1 that is second closest to the diagonal. The resonances sweep through most of the plane below the diagonal at larger separations, suggesting that these short-duration PN evolutions may have failed to capture the full magnitude of the anti-alignment. We will investigate this possibility in Sec. IV.

Another interesting feature of Figs. 1 and 2 is that the red long-dashed curves along which the BBHs inspiral are nearly parallel to the dot-dashed green lines along which the projection $\mathbf{S}_0 \cdot \hat{\mathbf{L}}_N$ of the effective-one-body (EOB) spin [40]

$$\mathbf{S}_0 \equiv (1+q)\mathbf{S}_1 + (1+q^{-1})\mathbf{S}_2 \quad (3.4)$$

is constant. The conservation of this quantity at 2PN order was first noted in Ref. [33] and follows directly from Eqs. (2.1), (2.2), and (2.5). The conservation of $\mathbf{S}_0 \cdot \hat{\mathbf{L}}_N$ rather than $\mathbf{S} \cdot \hat{\mathbf{L}}_N$ itself allows for the possible alignment of the total spin \mathbf{S} discussed in the previous paragraph.

We conclude this Section by briefly discussing how the spin-orbit resonances vary with the mass ratio q , as can be seen by comparing the $q = 9/11$ resonances in Fig. 1 with the $q = 1/3$ resonances in Fig. 2. The most pronounced differences are that the $q = 1/3$ resonances sweep away from the edges of the $(\cos\theta_1, \cos\theta_2)$ plane at much smaller values of the separation r , and do not approach the diagonal as closely. This is consistent with the decreasing value of r_{lock} in Eq. (1.4) as $q \rightarrow 0$. In this limit both t_p and t_{GW} are proportional to q^{-1} , implying that generic BBHs will be less likely to be affected by the resonances as they sweep through the plane over a smaller range in r . BBHs already in a resonant configuration will also be less affected since the resonant curves do not approach the diagonal as closely. The red long-dashed curves showing the inspiral of resonant configurations have steeper slopes for $q = 1/3$, consistent with the larger black hole being immune to its smaller companion in the limit $q \rightarrow 0$. This seems to contradict the puzzling result presented in Table IV of Lousto *et al.* [27] that it is the *smaller* companion that remains randomly

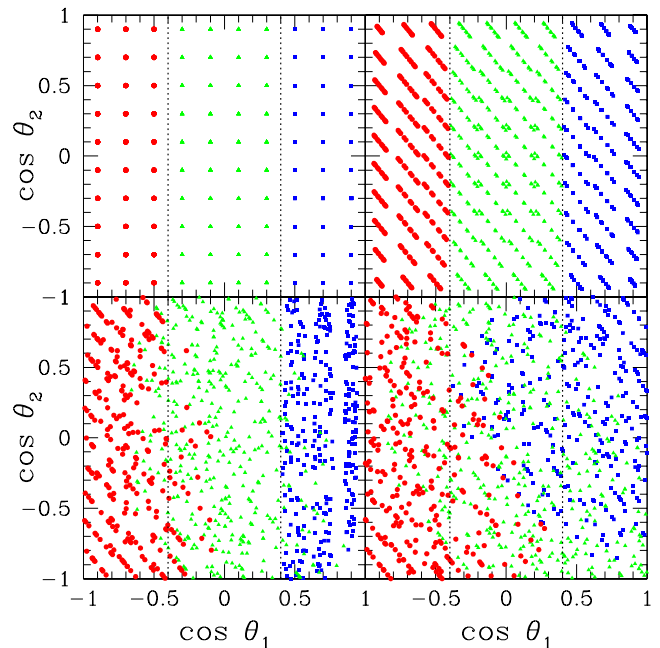


FIG. 3: Distributions of $(\cos\theta_1, \cos\theta_2)$ at different separations r for 1000 initially isotropic maximally spinning BBHs with a mass ratio $q = 9/11$. The top left panel shows the initial $10 \times 10 \times 10$ grid, evenly spaced in $(\cos\theta_1, \cos\theta_2, \Delta\phi)$. The dotted vertical lines show $\cos\theta_1 = \pm 0.4$. The 300 blue squares initially have $\cos\theta_1 > 0.4$, the 400 green triangles initially have $-0.4 < \cos\theta_1 < 0.4$, and the 300 red circles initially have $\cos\theta_1 < -0.4$. The values of (θ_1, θ_2) for these BBHs are shown in the top right, bottom left, and bottom right panels after they have inspiraled to separations of $r = 1000, 100$ and $10M$ respectively.

distributed during the inspiral. We will examine this behavior as well in the next Section.

IV. SPIN ALIGNMENT

In this Section, we examine the extent to which the spins of *generic* (i.e. misaligned) BBH configurations become aligned with the orbital angular momentum and each other as the BBHs inspiral from $r_i = 1000M$ to $r_f = 10M$. Although we use maximally spinning BBHs to demonstrate this alignment, the magnitude of the alignment is comparable for all BBHs with $\chi_{1,2} \gtrsim 0.5$ as shown in Fig. 11 of [25]. We first consider initial spin configurations given by a uniform $10 \times 10 \times 10$ grid evenly spaced in $(\cos\theta_1, \cos\theta_2, \Delta\phi)$. This distribution is isotropic, and would be expected in the absence of an astrophysical mechanism to align the spins. BBHs with isotropically oriented spins might form in gas-poor mergers of SBHs and mergers of stellar-mass black holes in dense clusters.

In Fig. 3, we show how the distribution of

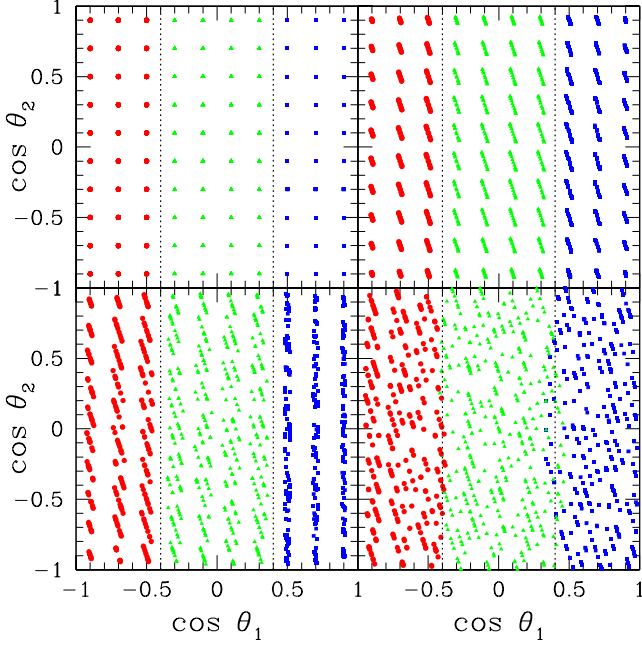


FIG. 4: Distributions of $(\cos \theta_1, \cos \theta_2)$ at different separations r for 1000 initially isotropic maximally spinning BBHs with a mass ratio $q = 1/3$. The different panels, points, and lines are the same as those given for $q = 9/11$ in Fig. 3.

$(\cos \theta_1, \cos \theta_2)$ evolves as maximally spinning BBHs with a mass ratio $q = 9/11$ inspiral from slightly beyond $r_i = 1000M$ to $r_f = 10M$. The top left panel shows our initial evenly spaced $10 \times 10 \times 10$ grid. The points are colored to indicate their *initial* value of $\cos \theta_1$: blue squares begin with $\cos \theta_1 > 0.4$ ($\theta_1 \lesssim 66^\circ$), green triangles with $-0.4 < \cos \theta_1 < 0.4$, and red circles with $\cos \theta_1 < -0.4$. The dotted vertical lines $\cos \theta = \pm 0.4$ denote these boundaries. Only 100 points are visible in the top left panel, as the different values of $\Delta\phi$ cannot be distinguished in this two-dimensional projection. Spin precession reveals all 1000 points after the BBHs have inspiraled to $r_i = 1000M$ as seen in the top right panel. Notice that the spins of all 1000 BBHs precess in a way that conserves the projection of \mathbf{S}_0 onto $\hat{\mathbf{L}}_N$ (parallel to the dot-dashed green lines in Fig. 1). This is not a special feature of the spin-orbit resonances, but occurs for generically oriented spins as well. These generic spin configurations do not individually preserve $(\cos \theta_1, \cos \theta_2)$ over a precession time t_p like the resonant configurations do, but they do preserve the combination $\mathbf{S}_0 \cdot \hat{\mathbf{L}}_N$. This precession continues as the BBHs inspiral to $r = 100M$ and $r_f = 10M$ as shown in the bottom left and bottom right panels of Fig. 3. By the time they reach $r_f = 10M$ the green points have diffused to fill most of the $(\cos \theta_1, \cos \theta_2)$ plane, while the blue (red) points have diffused into the upper right (lower left) portion of the middle $-0.4 < \cos \theta_1 < 0.4$ region. The bottom

right panel, if the points had not been colored, would reproduce Fig. 1 of Bogdanovic *et al.* [23] and therefore support their conclusion that isotropically distributed spins remain isotropic as they inspiral. However, the colors reveal that PN evolution can drastically alter spin distributions that have been partially aligned by a circumbinary disk. For example, if the spin of the more massive black hole was aligned so that $\cos \theta_1 > 0.4$ at $r_i = 1000M$ (shown by our blue points), by the time the binary reached $r_f = 10M$ the larger spin could easily lie in the orbital plane and thus give rise to a smaller final spin and potentially large “superkick” [15, 16].

For comparison, we show the inspiral of the same $10 \times 10 \times 10$ grid of maximally spinning BBHs with a mass ratio $q = 1/3$ in Fig. 4. The points diffuse along the steeper lines that preserve $\mathbf{S}_0 \cdot \hat{\mathbf{L}}_N$ for this less equal mass ratio. This inhibits their ability to diffuse across the $\cos \theta_1 = \pm 0.4$ boundaries, again shown by the vertical dotted lines. Even at $r_f = 10M$ only a few points have trickled between the three regions. Since the spin of the more massive black hole remains aligned with the orbital angular momentum, one would expect a large final spin and an absence of superkicks for such small mass ratios. We will examine in detail how spin alignment affects recoil-velocity distributions in future work.

In Fig. 5 we show how the joint probability distribution function for $\Delta\phi$ and $\cos \theta_{12}$ evolves for our evenly spaced $10 \times 10 \times 10$ grid of initially isotropic BBH spin configurations. As defined in the Introduction, $\cos \theta_{12}$ is the cosine of the angle between \mathbf{S}_1 and \mathbf{S}_2 . It can be expressed in terms of the individual spin angles as

$$\cos \theta_{12} = \sin \theta_1 \sin \theta_2 \cos \Delta\phi + \cos \theta_1 \cos \theta_2, \quad (4.1)$$

and has a flat distribution between -1 and 1 for isotropic, uncorrelated spins such as those given by our $10 \times 10 \times 10$ grid. However, as seen in Eq. (4.1), the values of $\cos \theta_{12}$ and $\cos \Delta\phi$ are correlated; for a given value of $\Delta\phi$ the distribution of $\cos \theta_{12}$ is peaked about $\cos \Delta\phi$ for flat distributions of $\cos \theta_1$ and $\cos \theta_2$. This can be seen in Fig. 5 from the clustering of points about the curve $\cos \theta_{12} = \cos \Delta\phi$. Although $\cos \theta_{12}$ and $\cos \Delta\phi$ are correlated even for isotropic spins, geometry implies that both are initially uncorrelated with the value of $\cos \theta_1$. This is revealed by the identical distributions of the red, green, and blue points in the top left panel of Fig. 5 to within the resolution of our grid. These distributions do not remain identical as the BBHs inspiral from $r_i = 1000M$ to $r_f = 10M$. Influenced by the $\Delta\phi = 0^\circ$ spin-orbit resonances below the diagonal in Fig. 1, the blue points become concentrated about $\Delta\phi = 0^\circ, \cos \theta_{12} = 1$ by the time they reach r_f . The red points, similarly influenced by the $\Delta\phi = \pm 180^\circ$ resonances above the diagonal in Fig. 1, become concentrated about $\Delta\phi = \pm 180^\circ, \cos \theta_{12} = -1$. The effect of this spin alignment on the spin of the final black hole will be explored in detail in the next Section, while the effect on recoil velocities will be examined in future work. Qualitatively, alignment of the spins with each other ($\cos \theta_{12} \rightarrow 1$) increases the final spin and reduces

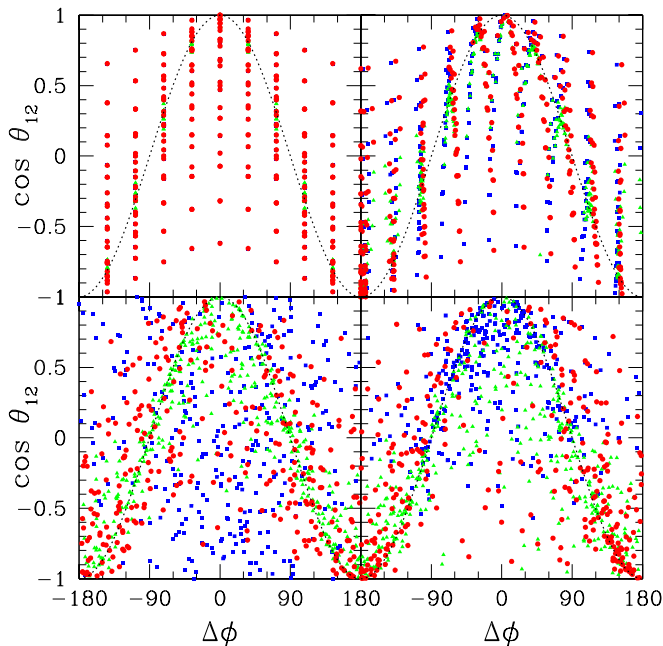


FIG. 5: Distributions of $(\Delta\phi, \cos\theta_{12})$ at different separations r for 1000 initially isotropic maximally spinning BBHs with a mass ratio $q = 9/11$. The top left panel shows the initial $10 \times 10 \times 10$ grid of BBH spin configurations, evenly spaced in $(\cos\theta_1, \cos\theta_2, \Delta\phi)$. This distribution is peaked about the curve $\cos\theta_{12} = \cos\Delta\phi$ shown by the dotted curve. The points are colored according to their initial values of $\cos\theta_1$ as in Fig. 3. The top right, bottom left, and bottom right panels show the distribution evolves after the BBHs have inspiraled to $r = 1000, 100$ and $10M$ respectively, also as in Fig. 3.

the recoil velocity, while anti-alignment ($\cos\theta_{12} \rightarrow -1$) does the opposite.

The magnitude of this spin alignment is greatly reduced for smaller mass ratios as seen in Fig. 6 for the case $q = 1/3$. Although the clustering of all the points about $\cos\theta_{12} = \cos\Delta\phi$ is again apparent, the distributions of the red, green, and blue points remain similar all the way down to $r_f = 10M$ as seen in the lower right panel. The weaker influence of the spin-orbit resonances for $q = 1/3$ follows from the smaller value of r_{lock} in Eq. (1.4), and is similarly reflected by the smaller fraction of the $(\cos\theta_1, \cos\theta_2)$ plane occupied by the resonant curves in Fig. 2.

We have provided histograms of $\cos\theta_{12}$ and $\Delta\phi$ in Fig. 7 to clarify the differences between Figs. 5 and 6. We see that the distributions of $\cos\theta_{12}$ and $\Delta\phi$ are initially flat for both mass ratios, but evolve considerably for $q = 9/11$ while remaining nearly flat for $q = 1/3$ within the limits set by Poisson fluctuations. The open blue (red) curves in the left panels of Fig. 7 clearly show distributions peaked at $\cos\theta_{12} = 1, \Delta\phi = 0^\circ$ ($\cos\theta_{12} = -1, \Delta\phi = \pm 180^\circ$). Such trends are barely noticeable in the right panels. We will explore the impli-

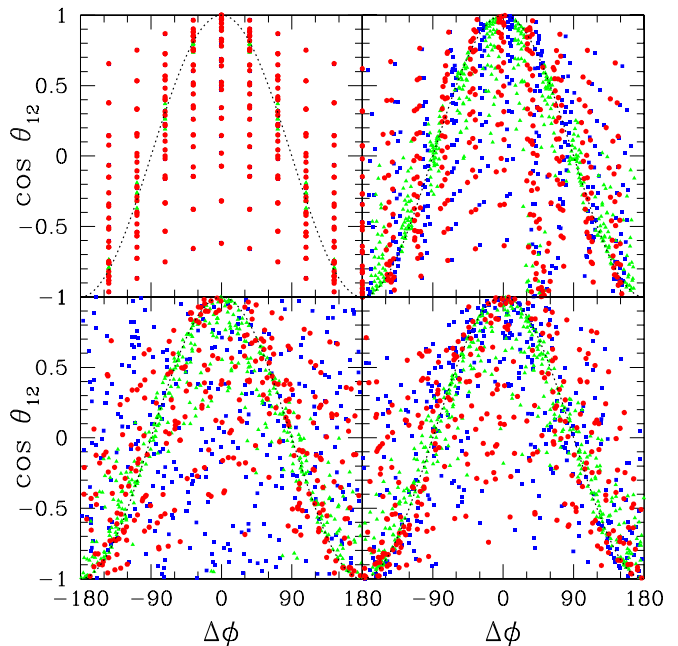


FIG. 6: Distributions of $(\Delta\phi, \cos\theta_{12})$ at different separations r for 1000 initially isotropic maximally spinning BBHs with a mass ratio $q = 1/3$. The different panels, points, and lines are the same as those given for $q = 9/11$ in Fig. 5.

cations of these findings for the final spins in the next Section.

V. FINAL SPIN DISTRIBUTIONS

Several attempts have been made to predict the final dimensionless spin χ_f of the black hole resulting from a BBH merger. Initial attempts focused on finding simple phenomenological fitting formulae for the final spin resulting from non-spinning, unequal-mass BBH merger simulations [41–43]. A group at the Albert Einstein Institute (AEI) developed a fitting formula that provides the magnitude and direction of χ_f in terms of the initial spins χ_1, χ_2 and the mass ratio q [44–46]. They assumed that the final spin magnitude could be expressed as a polynomial in χ_1, χ_2 , and the symmetric mass ratio η , then made some additional assumptions about the symmetries of this polynomial dependence and how energy and angular momentum are radiated to reduce the number of terms in their expression. The coefficients of the remaining terms were calibrated using numerical-relativity (NR) simulations of BBH mergers in which the initial spins were either aligned or anti-aligned with the orbital angular momentum. We shall refer to this older AEI formula as “AEIo”. A more recent paper [30] by members of this group uses newer NR simulations to recalibrate their coefficients, and replaces earlier assumptions with the con-

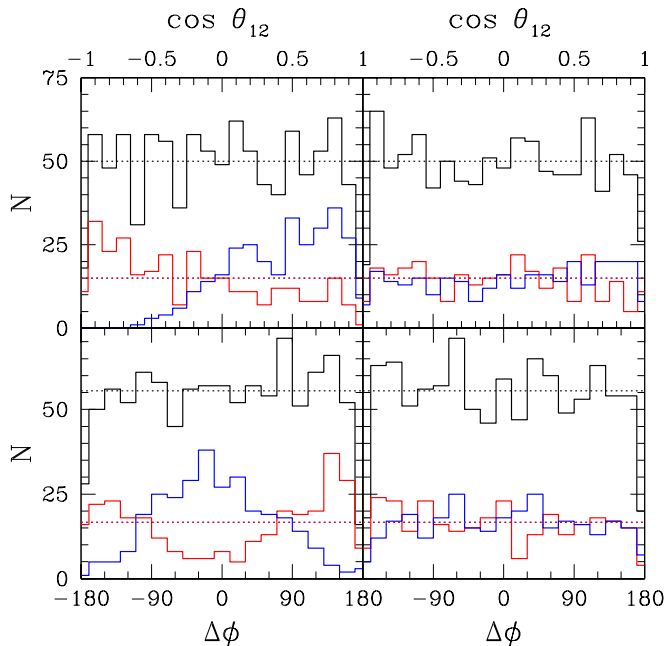


FIG. 7: Histograms of $\cos \theta_{12}$ and $\Delta\phi$ for BBHs with initially isotropic spins. The two left panels are for the mass ratio $q = 9/11$, while the two right panels are for $q = 1/3$. The two top panels give the distribution of $\cos \theta_{12}$, while the two bottom panels give the distribution of $\Delta\phi$. The black curves are for all 1000 BBHs in the $10 \times 10 \times 10$ grid discussed in the text, while the blue (red) curves correspond to the blue (red) points in Figs. 3-6 with initial values $\cos \theta_1 > 0.4$ ($\cos \theta_1 < -0.4$). The horizontal dotted lines show the initially flat distributions, while the solid lines show the distributions at $r = 10M$.

jecture that the final spin points in the direction of the total angular momentum of the initial BBH at *any* separation. For consistency, this requires the further assumption that angular momentum is always radiated in the direction of the total angular momentum. We shall refer to this newer AEIn formula as “AEIn”. An alternative fitting formula was proposed by a group at Florida Atlantic University (FAU) [47]. Following the procedure outlined in [38, 39], the FAU group performed 10 equal-mass misaligned simulations to calibrate the coefficients of fitting formulae for the Cartesian components of χ_f . They then made additional assumptions about the mass-ratio dependence of these formulae, and found good agreement between their predictions and independent NR simulations with mass ratios as small as $q = 5/8$. We shall refer to the formula of this group as “FAU”. The Rochester Institute of Technology (RIT) group proposed yet another fitting formula during the preparation of this paper [48]. This formula includes higher-order terms in the initial spins that may ultimately be needed to describe future high-accuracy NR simulations. However, current simulations are inadequate to calibrate all the terms appearing in the RIT formula, so we will not consider its predictions

in this paper.

Other groups have predicted final spins by extrapolating analytical test-particle calculations to finite mass ratios, rather than calibrating fitting formulae with NR simulations. Buonanno, Kidder, and Lehner (BKL) [49] derived a formula for the final spin by assuming, as is true in the test-particle limit, that the angular momentum radiated during the inspiral stage of a BBH merger exceeds that radiated during the plunge and ringdown. Using this assumption, they equated the final spin with the total angular momentum $\mathbf{J} = \mathbf{L}_{\text{ISCO}} + \mathbf{S}_1 + \mathbf{S}_2$, where \mathbf{L}_{ISCO} is the orbital angular momentum at the innermost stable circular orbit (ISCO) of a test particle of mass ηM orbiting a black hole of mass M and dimensionless spin χ_f equal to that of the *final* black hole. This counterintuitive but inspired choice correctly provides $\chi_f \rightarrow \chi_1$ in the $q \rightarrow 0$ limit and respects the symmetry of BBH mergers under exchange of the labels of the two black holes. Though derived only from test-particle calculations, the BKL formula is remarkably successful at predicting final spins even for equal-mass BBH mergers. Kesden [50] slightly modified the BKL spin formula to account for the energy radiated during the inspiral stage of the merger. This change makes the formula accurate to linear order in q in the test-particle limit. It generically increases the magnitude of the predicted dimensionless final spin by reducing the predicted final mass m_f below M in the denominator of the expression $\chi_f = S_f/m_f^2$. This increase improves the agreement with NR simulations of non-spinning BBH mergers, but leads to somewhat larger final spins than the other formulae for mergers of maximally spinning BBHs, such as those considered in this paper. The predictions of this formula are referred to as “Kes” in this paper.

We now present the predictions of the spin formulae summarized above for various distributions of BBH spins that are allowed to inspiral from $r_i = 1000M$ to $r_f = 10M$.

A. Spin Magnitudes

In the top panel of Fig. 8, we show the final spin magnitude χ_f predicted by the AEIn formula for the evenly spaced $10 \times 10 \times 10$ grid of maximally spinning BBHs with $q = 9/11$ described in Sec. IV. The other spin formulae give very similar results; the mean and variance of the final spin distributions predicted by the other formulae for some of the initial distributions described below are provided in Table I. As in Figs. 3-7, the black curves in Fig. 8 refer to all 1000 BBHs, the blue curves to the subset of 300 BBHs with the lowest values of θ_1 , and the red curves to the subset of 300 BBHs with the highest values of θ_1 . The dotted curves give the final spin distribution predicted for the BBH spin configurations at their initial separation $r_i = 1000M$, while the solid curves give the final spin distribution predicted when these *same* BBHs are allowed to inspiral to $r_f = 10M$.

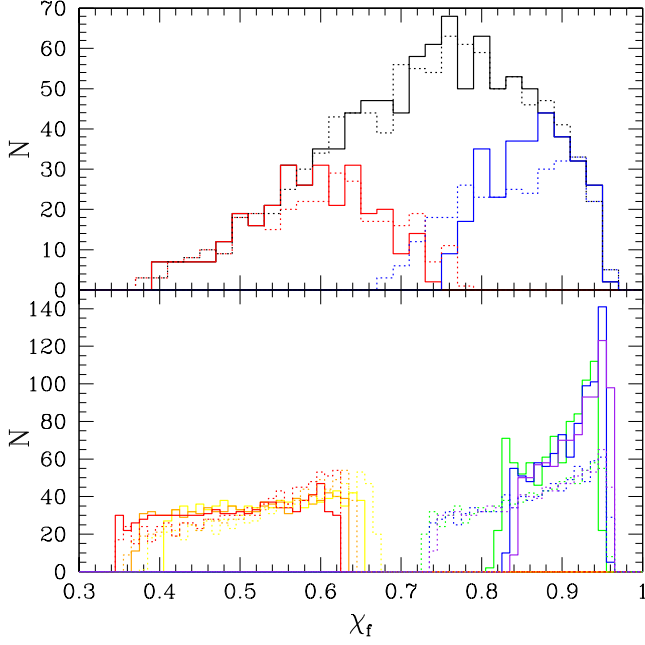


FIG. 8: *Top panel:* Histogram of the final spin χ_f predicted by the AEIn formula for 1000 BBHs with mass ratio $q = 9/11$ and isotropically distributed spins at $r_i = 1000M$. The blue curves show the subset of 300 BBHs with the lowest initial values of θ_1 , while the red curves show the subset of 300 BBHs with the highest initial values of θ_1 . The solid curves show the predicted spins if the AEIn formula is applied at $r_f = 10M$ after the BBHs have inspiraled to this separation according to the equations of Sec. II. The dotted curves show the predicted spins if the AEIn formula is applied to the initial distribution at $r_i = 1000M$. *Bottom panel:* Histograms of the predicted final spins for 6 sets of BBH mergers with $q = 9/11$, and flat distributions in $\cos\theta_2$ and $\Delta\phi$ at $r_i = 1000M$. The red, orange, yellow, green, blue, and purple curves have $\theta_1 = 170^\circ, 160^\circ, 150^\circ, 30^\circ, 20^\circ$, and 10° respectively. As in the top panel the final spins predicted by applying the AEIn formula at $r_i = 1000M$ are shown by dotted curves, while allowing the BBHs to inspiral to $r_f = 10M$ before applying the formula leads to the spins shown by the solid curves.

according to the PN evolution described in Sec. II. The AEIn formula is unique in that it claims to accurately predict final spins at all separations; separations as large as $r = 2 \times 10^4 M$ were considered in [30]. The other fitting formulae were intended to apply at $r_{NR} \simeq 10M$, the starting point for the NR simulations with which their coefficients were calibrated. The BKL and Kes formulae were designed for use at the ISCO. Although strictly speaking the formulae other than AEIn cannot be applied to widely separated BBHs, one can imagine that the BBHs inspiral to $r_f = 10M$ without spin precession where these formulae are valid. It is in this sense that we consider the predictions of these other formulae when we claim in this Section to apply them to BBH spin configuration at $r_i = 1000M$.

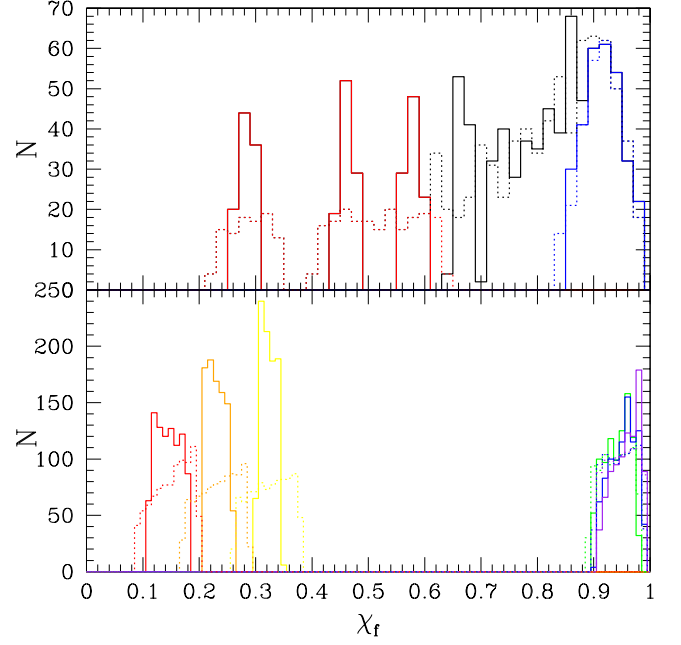


FIG. 9: Histograms of the final spins χ_f predicted by the AEIn formula for the same sets of BBHs presented in Fig. 8, but with the mass ratio $q = 1/3$ instead of $q = 9/11$. As in that figure, the predictions made at $r_i = 1000M$ are shown with dotted curves, those made at $r_f = 10M$ are shown with solid curves. The black curves in the top panel show the full set of 1000 BBHs, while the blue (red) curves show the subset of 300 BBHs with the lowest (highest) initial values of θ_1 . In the lower panel, the red, orange, and yellow curves show BBHs with χ_1 initially anti-aligned with \mathbf{L}_N ($\theta_1 = 170^\circ, 160^\circ, 150^\circ$). The green, blue, and purple curves show BBHs with χ_1 initially aligned with \mathbf{L}_N ($\theta_1 = 30^\circ, 20^\circ, 10^\circ$).

The dotted and solid black curves in the top panel of Fig. 8 are identical to within the Poisson noise of our limited number of BBH inspirals, confirming the finding of Refs. [23, 26, 27] that isotropic distributions of BBH spins remain nearly isotropic as they inspiral. Even at $r_i = 1000M$, the blue (red) subset of spin configurations yields the largest (smallest) predicted final spins, because for these configurations the spin of the more massive black hole is aligned (anti-aligned) with the orbital angular momentum. The spin-orbit resonances further enhance (reduce) the final spins predicted for these subsets by aligning (anti-aligning) the BBH spins *with each other* during the inspiral for small (large) initial values of θ_1 . As a result, the solid blue (red) distribution at $r_f = 10M$ has a larger (smaller) mean final spin than the initial dotted distribution at $r_i = 1000M$. This can be seen in the displacement of predicted final spins for the colored subsets away from $\chi_f \simeq 0.75$ towards larger and smaller values.

To clarify the magnitude of this effect, we have performed 6 additional sets of BBH inspirals, each of which

consists of a fixed value of θ_1 and a 30×30 grid evenly spaced in $\cos\theta_2$ and $\Delta\phi$. Three of these sets have the spin of the more massive black hole nearly aligned with the orbital angular momentum ($\theta_1 = 10^\circ, 20^\circ, 30^\circ$), while the other 3 sets have χ_1 nearly anti-aligned with \mathbf{L}_N ($\theta_1 = 150^\circ, 160^\circ, 170^\circ$). The choice of aligned distributions was partly motivated by the finding of Ref. [17] that accretion torques will align BBH spins to within 10° (30°) of the orbital angular momentum for a cold (hot) disk. The predicted final spins for these distributions, both at $r_i = 1000M$ and $r_f = 10M$, are shown in the bottom panel of Fig. 8. The final spins for the initially aligned ($\theta_1 \leq 30^\circ$) BBH distributions are significantly larger when predicted at $r_f = 10M$ than at $r_i = 1000M$, undermining the claim of [30] that the AEIn formula can accurately predict final spins at large separations without the need for PN evolutions. The predicted final spins for the initially anti-aligned ($\theta_1 \geq 150^\circ$) BBH distributions conversely shift to lower values as the predictions are made later in the inspiral. We provide the mean and standard deviation of the final spins predicted for these 6 new sets of partially aligned BBH distributions for all 5 formulae in Table I.

To explore the dependence of these effects on the mass ratio, we have provided histograms of the predicted final spins for these same BBH spin distributions with $q = 1/3$ in Fig. 9. The discrete peaks at low values of χ_f in the histograms in the top panel are an artifact of the 10 discrete values of $\cos\theta_1$ in our $10 \times 10 \times 10$ grid. Each peak contains 100 points with the same initial value of θ_1 . The decrease in the width of each peak as the BBHs inspiral from $r_i = 1000M$ to $r_f = 10M$ is a consequence of the anti-alignment of the BBH spins for large θ_1 , but the gaps between the peaks would be filled in if we used a finer grid. The shifts in the mean values of the peaks should be robust with respect to the grid spacing. These shifts for the initially aligned BBH distributions are provided in Table I for all 5 formulae for $q = 1/3$, as well as for the intermediate mass ratio $q = 2/3$.

B. Spin Directions

Before providing quantitative results, we need to clarify what is meant by the *direction* of the spin of the final black hole. In what reference frame is this direction defined? Most of the fitting formulae calibrated with NR simulations attempt to predict the angle

$$\vartheta_f \equiv \arccos[\hat{\mathbf{L}}_N(r_f) \cdot \hat{\chi}_f(r_f)] \quad (5.1)$$

between the BBH orbital angular momentum \mathbf{L}_N at the separation $r_f = r_{\text{NR}}$ where the NR simulations were performed and the final spin χ_f predicted from the BBH spin configuration at this *same* separation. The analytical predictions of BKL and Kes were designed to apply to BBH spin configurations at $r_f = r_{\text{ISCO}}$. If one assumed that neither the orbital angular momentum nor the BBH

spins (upon which the prediction $\hat{\chi}_f(r_f)$ depends) precess during the inspiral, one could insert these quantities *at any separation* into the right-hand side of Eq. (5.1) to predict ϑ_f . The angle ϑ_f is physically interesting because it quantifies the post-merger alignment between χ_f and the inner edge of the accretion disk if one assumes that torques have aligned the circumbinary disk with \mathbf{L}_N . However, one might also be interested in the alignment between χ_f and a feature like the galactic disk that is assumed to be aligned with \mathbf{L}_N at some larger scale r_i . In that case, one would need to compute the angle

$$\vartheta_i \equiv \arccos[\hat{\mathbf{L}}_N(r_i) \cdot \hat{\chi}_f(r_i)] \quad (5.2)$$

between \mathbf{L}_N at this larger separation and the final spin $\chi_f(r_i)$ predicted from the BBH spins at this same separation.

The proper way to predict χ_f from the BBH spins at r_i would be to use PN equations like those specified in Sec. II to propagate those spins and \mathbf{L}_N to down to r_f , then insert them into the fitting formula of one's choice. The AEIn formula is based on the conjecture that χ_f points in the direction of the total angular momentum \mathbf{J} at *any* separation, since angular momentum is always radiated parallel to \mathbf{J} , thus preserving its direction. This conjecture is plausible because at large separations, the precession time t_p is much shorter than the inspiral time t_{GW} . If the vectors associated with the BBHs precess rapidly enough, all components except those parallel to \mathbf{J} (which varies on the longer timescale t_{GW}) will average to zero. The AEIn conjecture is very useful because it allows ϑ_i to be computed without solving any PN equations. However, the approximation $t_p \ll t_{\text{GW}}$ upon which it depends breaks down at small separations. This may lead to incomplete cancellation of the angular momentum radiated perpendicular to \mathbf{J} .

We test this possibility by calculating

$$\theta_J \equiv \arccos[\hat{\mathbf{J}}(r_i) \cdot \hat{\mathbf{J}}(r_f)] , \quad (5.3)$$

the angle between the total angular momentum at $r_i = 1000M$ and that after the BBHs have inspiraled to $r_f = 10M$. If the direction of \mathbf{J} really was preserved during the inspiral, θ_J would vanish. We present histograms of θ_J for mass ratio $q = 9/11$ in Fig. 10. The upper panel shows the $10 \times 10 \times 10$ grid of BBH spin configurations evenly spaced in $(\cos\theta_1, \cos\theta_2, \Delta\phi)$ that we have discussed previously. The direction of \mathbf{J} changes by $\theta_J \lesssim 2^\circ$ during most of the inspirals, though a tail extends to larger values for large initial values of θ_1 . This tail can be seen more clearly in the bottom panel for the BBHs with χ_1 initially anti-aligned with \mathbf{L}_N ($\theta_1 \geq 150^\circ$). We agree with [30] that these large changes in the direction of \mathbf{J} are likely a consequence of the transitional precession first identified in Ref. [51]. This transitional precession occurs to an even greater extent for smaller mass ratios, as can be seen in Fig. 11 for $q = 1/3$. As in the upper panel of Fig. 9, discrete peaks resulting from the grid spacing in $\cos\theta_1$ can be seen in the left panel of Fig. 11. The middle panel shows that the direction of \mathbf{J} remains nearly

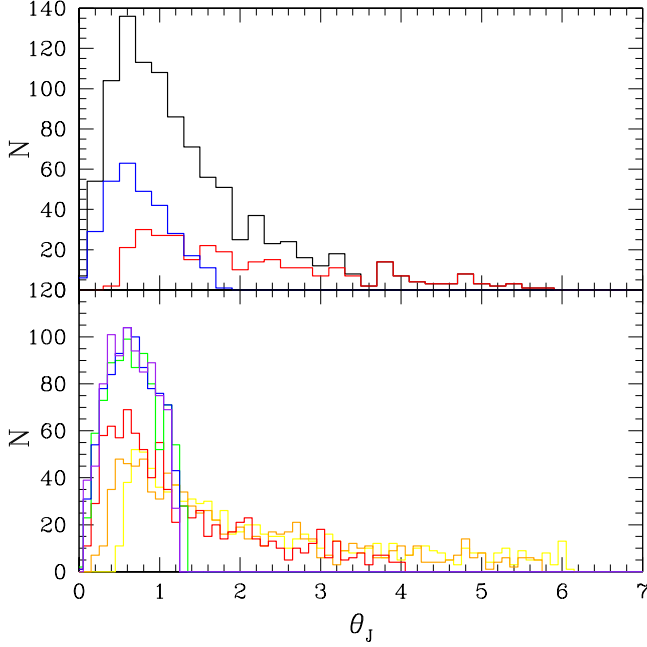


FIG. 10: *Top panel:* Histogram of the angle θ_J (in degrees) between the total angular momentum \mathbf{J} at $r_i = 1000M$ and that at $r_f = 10M$ for our set of 1000 BBHs with $q = 9/11$ and initially isotropic spins. As in previous figures, the blue (red) curve shows the subset of 300 BBHs with the lowest (highest) initial values of θ_1 . *Bottom panel:* Histograms of θ_J for the 6 sets of 900 BBH mergers with flat distributions in $\cos \theta_2$ and $\Delta \phi$ at $r_i = 1000M$. The red, orange, yellow, green, blue, and purple curves show BBHs that have $\theta_1 = 170^\circ, 160^\circ, 150^\circ, 30^\circ, 20^\circ$, and 10° respectively at this initial separation.

constant ($\theta_J \lesssim 0.5^\circ$) when χ_1 is closely aligned with \mathbf{L}_N ($\theta_1 \leq 30^\circ$). However, the right panel shows that the assumption of constant $\hat{\mathbf{J}}$ fails badly for the BBHs with $\theta_1 \geq 150^\circ$, that comprise $\sim 7\%$ of isotropically distributed BBH mergers. The mass ratio $q = 1/3$ is not extreme compared to the majority of astrophysical mergers, so caution should be taken when assuming that χ_f points in the direction of \mathbf{J} such as in Eq. (5.2).

What about the less ambitious predictions of ϑ_f from BBH spins at $r_f = 10M$, assuming that NR simulations correctly describe spin precession from this separation until merger? Spin-orbit resonances have significant implications for these predictions as well. We show predictions of ϑ_f by the AEIn formula for a mass ratio of $q = 9/11$ in Fig. 12. The other formulae predict very similar results. As in Figs. 8 and 9, the dotted curves show predictions assuming that the initial BBH spin distribution is preserved down to $r_f = 10M$. The solid curves include spin precession from $r_i = 1000M$ to $r_f = 10M$ according to the PN equations of Sec. II. The difference between the dotted and solid black curves in the top panel is below the Poisson fluctuations, another con-

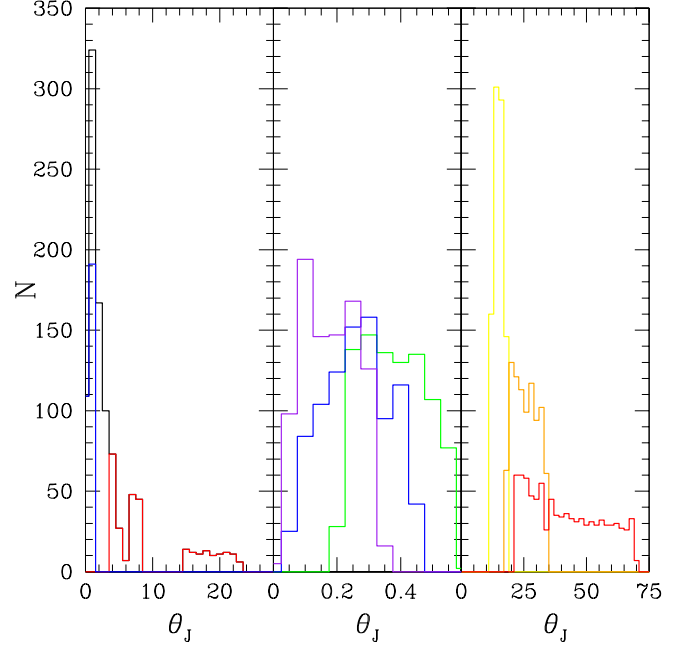


FIG. 11: *Left panel:* Histogram of the angle θ_J (in degrees) between the total angular momentum \mathbf{J} at $r_i = 1000M$ and that at $r_f = 10M$ for our set of 1000 initially isotropically spinning BBHs with $q = 1/3$. As in previous figures, the blue (red) curve shows the subset of 300 BBHs with the lowest (highest) initial values of θ_1 . *Middle panel:* Histograms of θ_J for the 3 sets of 900 BBH mergers initially with $\theta_1 = 10^\circ$ (purple), 20° (blue), and 30° (green). *Right panel:* Histograms of θ_J for the 3 sets of 900 BBH mergers initially with $\theta_1 = 150^\circ$ (yellow), 160° (orange), and 170° (red).

sequence of the finding of Refs. [23, 26, 27] that isotropically oriented BBH spins remain nearly isotropic as they inspiral. Careful examination of the upper panel reveals that spin precession has shifted the BBHs with χ_1 initially aligned with \mathbf{L}_N (blue distribution) to larger ϑ_f , while the anti-aligned BBHs have conversely shifted to smaller ϑ_f .

This trend is much more pronounced in the middle and bottom panels of Fig. 12. Spin precession actually results in the initially aligned BBHs ($\theta_1 \leq 30^\circ$) having larger values of ϑ_f at $r_f = 10M$ than the anti-aligned BBHs ($\theta_1 \geq 150^\circ$), a reversal of what would be predicted from the initial spin distributions shown by the dotted curves. The spin-orbit resonances explain this highly counterintuitive result. The BBHs initially with $\theta_1 \leq 30^\circ$ are influenced by the $\Delta \phi = 0^\circ$ resonances which align the BBH spins with each other and anti-align $\mathbf{S} = \mathbf{S}_1 + \mathbf{S}_2$ with \mathbf{L}_N . Both effects lead to larger predicted values of ϑ_f . Conversely, the BBHs initially with $\theta_1 \geq 150^\circ$ are influenced by the $\Delta \phi = 180^\circ$ resonances, which greatly decrease the magnitude of \mathbf{S} and align it with \mathbf{L}_N . This explains the reduced values of ϑ_f for these BBHs seen in the bottom panel of Fig. 12. This same effect can

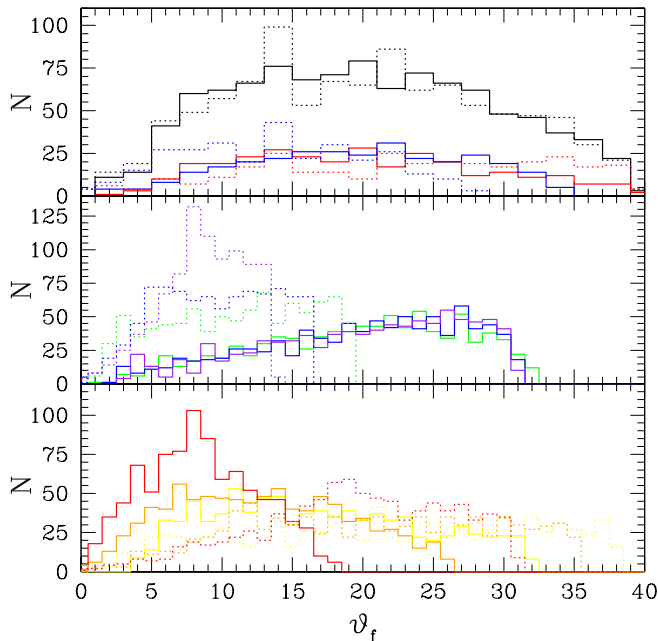


FIG. 12: *Top panel:* Histogram of the angle ϑ_f (in degrees) between the orbital angular momentum \mathbf{L}_N at $r_f = 10M$ and the final spin χ_f predicted by the AEIn formula from the BBH spins at that separation. The BBHs have a mass ratio $q = 9/11$. As in previous figures, the black curves show 1000 mergers with initially isotropic BBH spins, while the blue (red) curves show the subset of 300 BBHs with the lowest (highest) initial values of θ_1 . The dotted curves show predictions in the absence of spin precession, while the solid curves show how these predictions change when the BBH spins precess from $r_i = 1000M$ to $r_f = 10M$ according to the PN equations of Sec. II. *Middle panel:* Histograms of ϑ_f for the 3 sets of 900 BBH mergers with χ_1 initially aligned with \mathbf{L}_N [$\theta_1 = 10^\circ$ (purple), 20° (blue), 30° (green)]. *Bottom panel:* Histograms of ϑ_f for the 3 sets of 900 BBH mergers with χ_1 initially anti-aligned with \mathbf{L}_N [$\theta_1 = 150^\circ$ (yellow), 160° (orange), 170° (red)].

be seen for a mass ratio of $q = 1/3$ in Fig. 13, albeit with less significance owing to the weaker resonances at this smaller mass ratio. Figs. 12 and 13 again illustrate the importance of accounting for spin precession between $r_i = 1000M$ and $r_f = 10M$ when attempting to predict final spins.

VI. SPIN PRECESSION UNCERTAINTY

So far, we focused on how spin precession between r_i and r_f alters the expected distribution of final spins. In this Section, we show that spin precession introduces a fundamental uncertainty in predicting the final spin. An uncertainty Δr in the BBH separation leads to an uncertainty Δt_{GW} in the time until merger. If this uncertainty is comparable to the precession time t_p , the phase of the

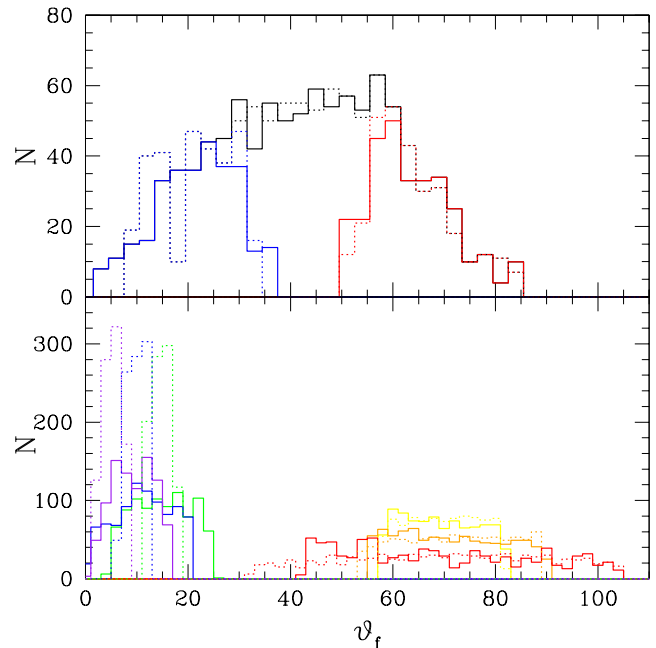


FIG. 13: Histograms of the angle ϑ_f predicted by the AEIn formula for the same sets of BBHs shown in Fig. 12 but with a mass ratio $q = 1/3$. As in that figure, the top panel shows BBHs with initially isotropic spins with the blue (red) curves indicating those BBHs with the lowest (highest) initial values of θ_1 . Dotted curves show predictions without spin precession, while the solid curves show how these predictions change if the BBHs spins precess from $r_i = 1000M$ to $r_f = 10M$ according to the PN equations of Sec. II. The bottom panel shows distributions with flat initial distributions of $\cos \theta_2$ and $\Delta \phi$, but with θ_1 now initially set to 170° , 160° , 150° , 30° , 20° , and 10° respectively for the red, orange, yellow, green, blue, and purple curves.

spin precession at which the merger occurs will be uncertain as well. This new uncertainty is independent of and may exceed that associated with the NR simulations themselves. Readers only interested in astrophysical distributions of final spins may wish to proceed to the discussion in Sec. VII.

It is often useful to define the final spin direction relative to the orbital angular momentum \mathbf{L}_N at different separations. We therefore generalize the angles defined in Eqs. (5.1) and (5.2) to the separation-dependent quantities

$$\vartheta_f(r) \equiv \arccos[\hat{\mathbf{L}}_N(r) \cdot \hat{\chi}_f(r)], \quad (6.1)$$

$$\vartheta_i(r) \equiv \arccos[\hat{\mathbf{L}}_N(r_i) \cdot \hat{\chi}_f(r)]. \quad (6.2)$$

Note that these quantities reduce to the previously defined angles in the appropriate limit: $\vartheta_f(r_f) = \vartheta_f$, $\vartheta_i(r_i) = \vartheta_i$. These definitions address two ambiguities; (i) the choice of the reference orbital angular momentum and (ii) the separation at which a given fitting formula is evaluated.

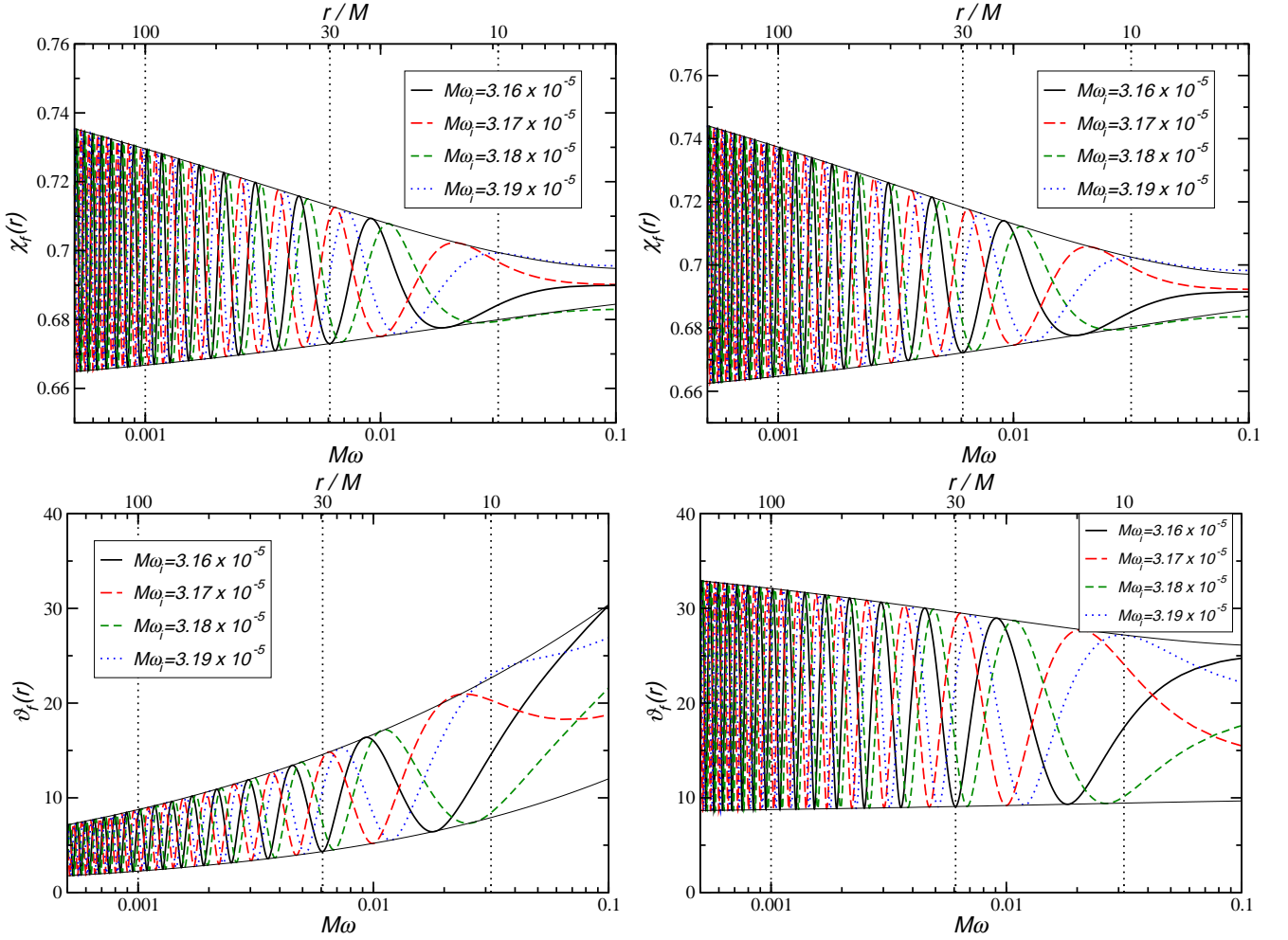


FIG. 14: Predicted χ_f (upper panels) and $\vartheta_f(r)$ (lower panels) obtained from the AEIn (left) and the Kesden (right) formula. The initial parameters of the binary are $q = 9/11$, $\chi_1 = \chi_2 = 1$, $\theta_1 = 120^\circ$, $\theta_2 = 60^\circ$ and $\Delta\phi = 288^\circ$. The different curves correspond to initial frequencies $M\omega_i = 3.16 \times 10^{-5}$ (solid), 3.17×10^{-5} (long-dashed), 3.18×10^{-5} (dashed) and 3.19×10^{-5} (dotted). The envelope determined for $M\omega_i = 3.16 \times 10^{-5}$ is displayed by thin solid curves. The upper horizontal axis gives the binary separation in units of M ; the lower horizontal axis gives the corresponding orbital frequency $M\omega$.

Before we discuss the uncertainties in determining these angles and the final spin magnitude, we illustrate the evolution of these quantities during the PN inspiral for a few characteristic examples. In Fig. 14 we display the final spin magnitude $\chi_f(r)$ and the angle $\vartheta_f(r)$ as predicted by the AEIn and the Kesden formulae for a binary with mass ratio $q = 9/11$, extremal spins, and initial spin orientation specified by the angles $\theta_1 = 120^\circ$, $\theta_2 = 60^\circ$, $\Delta\phi = 288^\circ$. The behavior of the AEIn, FAU and BKL formulae is quite similar to the Kesden formula. The different curves in each panel correspond to slightly different initial frequencies or separations, $M\omega_i = 3.16 \times 10^{-5}$, 3.17×10^{-5} , 3.18×10^{-5} and 3.19×10^{-5} . The spin precession generically manifests itself in the oscillatory character of the curves; these oscillations would be absent for the resonant configurations described in Sec. III. The thin solid lines represent *envelope* functions obtained by fitting fourth-order poly-

nomials to the maxima and minima, respectively, of the evolutions starting with $M\omega_i = 3.16 \times 10^{-5}$. Note that these fits contain no information on the results obtained by using different values of $M\omega_i$, and yet they still provide excellent envelopes in all cases.

This figure illustrates two ambiguities in predicting χ_f : (i) the *initial* frequency ω_i at which the BBH parameters are specified, and (ii) the *final* separation r_f at which the given formula for χ_f should be applied. Uncertainty in the separation at which the binary decouples from external interactions could lead to ambiguity in ω_i in theoretical studies, while uncertainty in the observed distance, projected separation, or line-of-sight velocity could lead to uncertainty in ω_i for models of particular systems. Gauge-dependent definitions of r_f could lead to uncertainty in the separation at which fitting formulae should be applied. Our task in evaluating the resulting uncertainties for the fitting formulae AEIn, AEIo, FAU, BKL

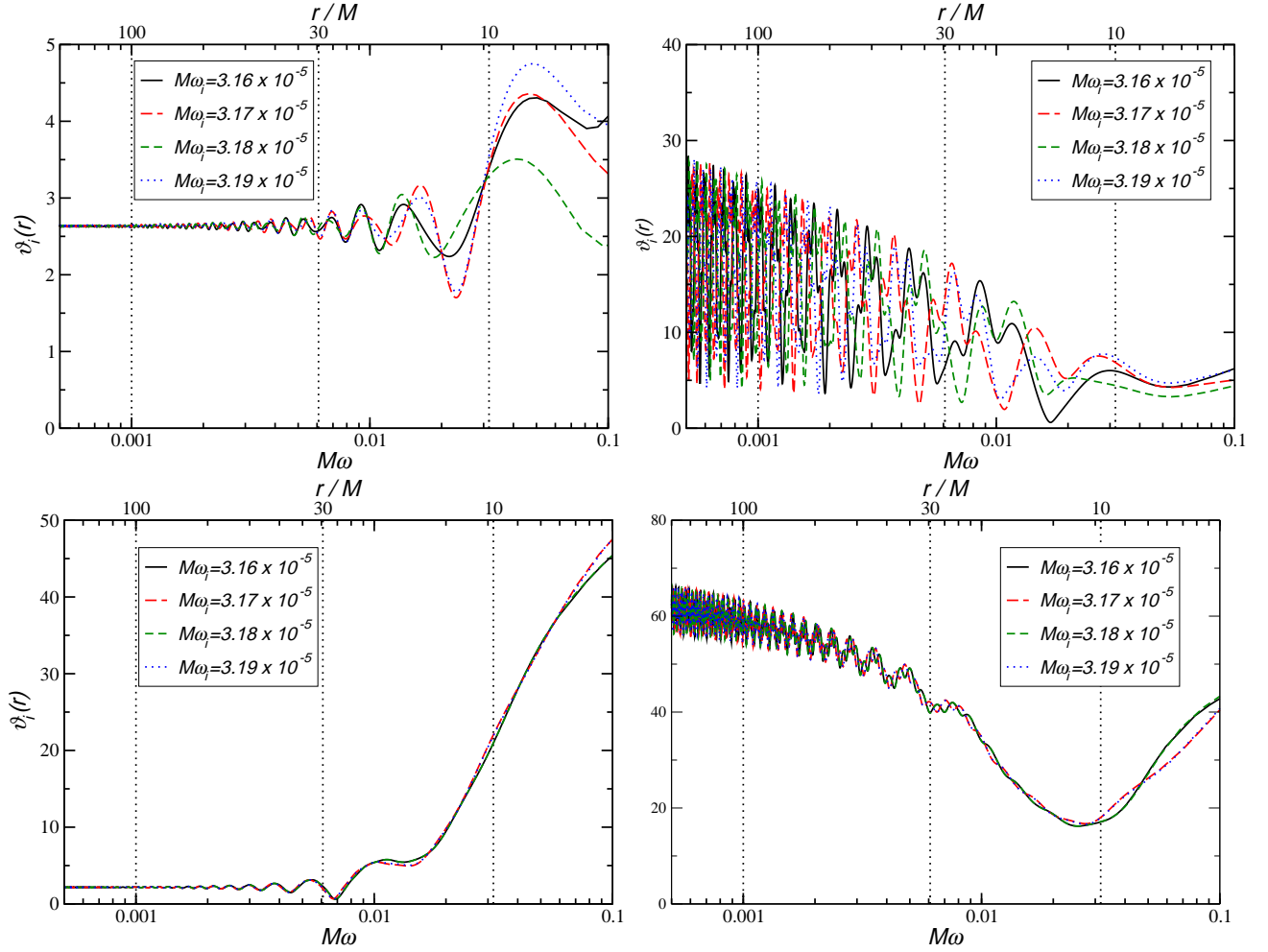


FIG. 15: Predicted spin direction $\vartheta_i(r)$ from the AEIn (left panels) and the Kes (right panels) formula. The upper panel shows the evolution of a binary starting with initial parameters $q = 9/11$, $\chi_1 = \chi_2 = 1$, $\theta_1 = 120^\circ$, $\theta_2 = 60^\circ$ and $\Delta\phi = 288^\circ$, as in Fig. 14. For comparison, in the bottom panels we consider a mass ratio $q = 1/3$ and initial spin parameters $\chi_1 = \chi_2 = 1$, $\theta_1 = 154^\circ$, $\theta_2 = 124^\circ$ and $\Delta\phi = 216^\circ$. The initial frequency is $M\omega_i = 3.16 \times 10^{-5}$ (solid), 3.17×10^{-5} (long-dashed), 3.18×10^{-5} (dashed) and 3.19×10^{-5} (dotted curve). The upper horizontal axis gives the binary separation in units of M ; the lower horizontal axis gives the corresponding orbital frequency $M\omega$.

and Kes introduced in Sec. V is somewhat simplified because both ambiguities are rooted in the rapid variations of the phase and in the resulting oscillations in the final quantities. These precession-induced oscillations are a clear manifestation of the hierarchy of time scales introduced in Eq. (3.1): $t_p \ll t_{\text{GW}}$.

In the upper panels of Fig. 15 we show the angle $\vartheta_i(r)$ for the same binary configuration illustrated in Fig. 14. In the lower panel of Fig. 15 we consider instead, for comparison, a system with lower mass ratio $q = 1/3$ and initial spin orientation $\theta_1 = 154^\circ$, $\theta_2 = 124^\circ$, $\Delta\phi = 216^\circ$. As before, different curves correspond to different initial frequencies. The predicted spin direction as described by $\vartheta_i(r)$ shows little variation with ω_i . On the other hand, the figure demonstrates a strong dependence of $\vartheta_i(r)$ on the separation r at which we apply the fitting formulae.

In the remainder of this Section, we discuss the uncer-

tainties caused by the rapid spin precession of the following quantities:

- 1) $\chi_f(r_f)$: The magnitude of the final spin as predicted by applying a given fitting formula at small binary separation $r_f = 10M$, i.e. shortly before merger.
- 2) $\vartheta_f(r_f)$: The angle between the orbital angular momentum at $r_f = 10M$ and the final spin (as predicted using the binary parameters at $r_f = 10M$).
- 3) $\vartheta_i(r_f)$: The angle between the orbital angular momentum of the binary at large separation and the final spin (as predicted using the binary parameters at $r_f = 10M$).
- 4) $\vartheta_i(r_i)$: The angle between the orbital angular momentum of the binary at large separation and the

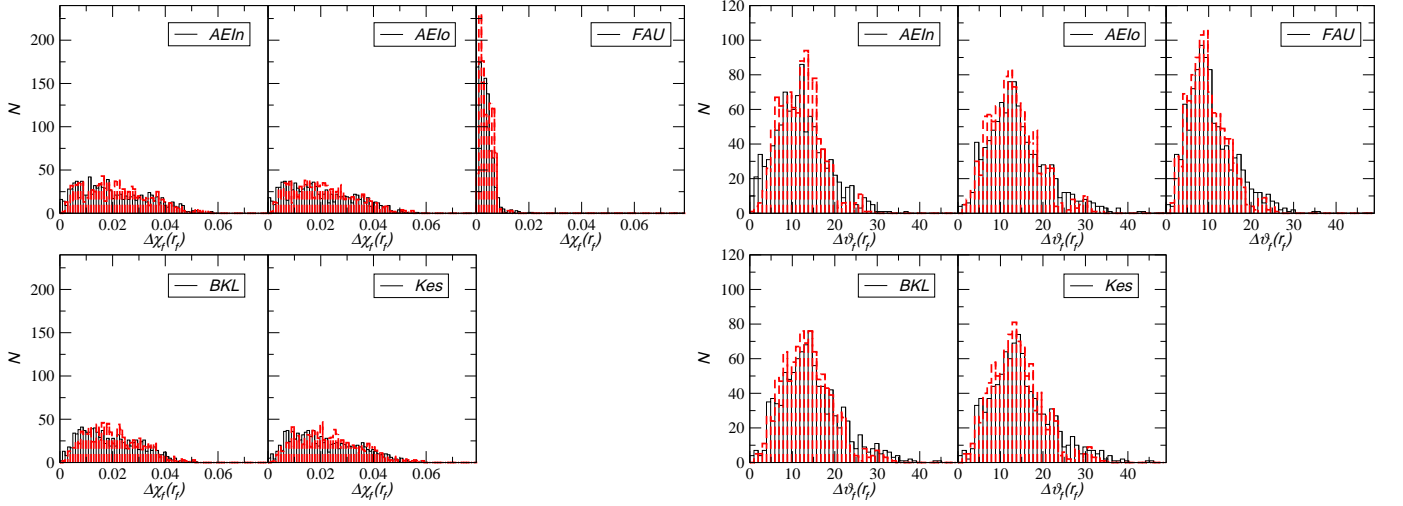


FIG. 16: Uncertainties in the final spin magnitude $\chi_f(r_f)$ (left) and direction $\vartheta_f(r_f)$ (right) for extremal BBHs with mass ratio $q = 2/3$. Solid black histograms were obtained by starting the evolutions at $M\omega_i = 3.16 \times 10^{-5}$ and using the envelope method of Fig. 14. Dashed red histograms were obtained by considering the maximum variation in the final quantities as we let $M\omega_i$ vary from 3.16×10^{-5} to 3.22×10^{-5} in steps of 0.005×10^{-5} .

final spin predicted using the binary parameters at this same large separation. We investigate the claim that the AEIn formula, unlike the others, can determine this angle without evolving the BBH parameters down to r_f .

These quantities are important for modeling the assembly of supermassive black holes in the context of cosmological structure formation (see e.g. [24, 52–56]). They are also relevant for electromagnetic counterparts of gravitational-wave sources [57], especially when the invoked mechanism producing the counterparts depends on the recoil velocity of the remnant black hole [58–60].

We determine the precession-induced uncertainties as follows. Individual evolutions, such as those considered in Fig. 14, suggest that the width of the envelopes or the dispersion induced by varying the initial frequency provide very similar estimates for the uncertainty in $\chi_f(r_f)$ and $\vartheta_f(r_f)$. We have verified this conjecture by evolving the evenly spaced $10 \times 10 \times 10$ grid of initially isotropic, maximally spinning BBH configurations introduced in Sec. IV for mass ratio $q = 2/3$ and several slightly different initial frequencies. When we estimate uncertainties by varying $M\omega_i$ from 3.16×10^{-5} to 3.22×10^{-5} in steps of 0.005×10^{-5} we obtain the red dashed histograms in Fig. 16. These histograms are in good agreement with the black solid histograms, where the uncertainty was estimated from the width of the envelopes. In order to reduce computational cost, in the remainder of this Section we determine the uncertainties $\Delta\chi_f(r_f)$ and $\Delta\vartheta_f(r_f)$ by evolving an ensemble of binaries from a *single* initial frequency ($M\omega_i = 3.16 \times 10^{-5}$) and using the envelope method.

Fig. 15 shows that the envelope method does not adequately describe the uncertainty in $\vartheta_i(r)$. Why does this angle behave so differently from $\vartheta_f(r)$ as illustrated in

Fig. 14? The direction of $\hat{\mathbf{L}}_N(r_i)$ is fixed, while according to the AEIn formula $\hat{\chi}_f(r)$ points in the direction of $\hat{\mathbf{J}}(r)$. The total angular momentum \mathbf{J} only varies on the radiation timescale t_{GW} , so according to Eq. (6.2) the AEIn prediction of $\vartheta_i(r)$ should only vary on this slower timescale as well. The left panels of Fig. 15, at least at small orbital frequencies $M\omega$ where $t_p \ll t_{\text{GW}}$, indeed lack the high-frequency oscillations characteristic of spin precession. In contrast, the Kesden predictions for $\vartheta_i(r)$ shown in the right panels of Fig. 15 are varying in a more complicated way than the predicted values of $\vartheta_f(r)$. Changes in the angle $\vartheta_i(r)$ between the fixed $\hat{\mathbf{L}}_N(r_i)$ and varying $\hat{\chi}_f(r)$ reflect the full complexity of spin precession for misaligned, unequal-mass BBHs. The simpler variation in $\vartheta_f(r)$ occurs because both $\hat{\mathbf{L}}_N(r)$ and $\hat{\chi}_f(r)$ are jointly precessing about $\hat{\mathbf{J}}(r)$, albeit on the same short timescale t_p .

Since the envelope method fails for $\vartheta_i(r)$, we somewhat arbitrarily define the uncertainty $\Delta\vartheta_i(r_f)$ as the maximum deviation of $\vartheta_i(r)$ from $\vartheta_i(r_f = 10M)$ in the window $r_f < r < 2r_f$. This window covers approximately the range of initial separations within the reach of present and near-future numerical relativity simulations, while smaller separations must be excluded due to the breakdown of the PN expansion. The formulae other than AEIn do not claim to predict $\hat{\chi}_f$ from the BBH parameters at large separations. To apply these formulae correctly, one must evolve the BBH parameters inwards to r_f according to PN equations such as those in Sec. II before applying the formulae. This evolution requires significant additional effort, but if performed properly would only increase $\Delta\vartheta_i(r_i)$ above $\Delta\vartheta_i(r_f)$ by the uncertainty in the PN equations themselves. The uncertainty coming from PN evolutions could be quantified by comparing

different PN orders and pushing the calculation of spin contributions to higher order; such an analysis is beyond the scope of this paper. The AEIn formula is special in that it predicts $\vartheta_i(r_i)$ without this additional PN evolution. Since AEIn claims that both $\hat{\mathbf{L}}_N(r_i)$ and $\hat{\chi}_f(r)$ are independent of r , the uncertainty $\Delta\vartheta_i(r_i)$ for this formula is the maximum deviation from $\vartheta_i(r_f = 10M)$ over the *entire* interval $r_f < r < r_i$. Since the orbital angular momentum \mathbf{L}_N increasingly dominates over spin contributions in the sum $\mathbf{J} = \mathbf{L}_N + \mathbf{S}_1 + \mathbf{S}_2$ at large separations, \mathbf{L}_N has little opportunity to precess at large separations and the uncertainty $\vartheta_i(r_i)$ asymptotes to a constant value in this limit.

We have evolved the uniform $10 \times 10 \times 10$ grid of maximally spinning binaries introduced in Sec. IV for three different mass ratios: $q = 9/11$, $q = 2/3$ and $q = 1/3$. The average uncertainties (plus or minus their associated standard deviations) are summarized in Table II.

Errors in the final spin magnitudes due to the rapid spin precession are in the range $\Delta\chi_f \lesssim 0.03$ for all mass ratios. The FAU formula performs exceptionally well for nearly equal masses, although it deteriorates to the level of the other predictions for $q = 1/3$. We suspect that this is because several of the higher-order terms in η in the FAU formula are symmetric in the dimensionless spins χ_1, χ_2 , while physically one would expect the spin of the more massive black hole to be more important in the limit $q \rightarrow 0$. Overall however, all formulae are able to predict the spin magnitude with rather good accuracy.

The uncertainty $\Delta\vartheta_f(r_f)$ in the angle between the final spin and the orbital angular momentum shortly before merger is typically in the range of a few to 20 degrees. Investigation of the angular dependence of the spin uncertainties shows that the AEIn formula tends to behave better for initially aligned spins (small θ_1 and θ_2) and worse for anti-aligned cases. This is likely a consequence of anti-aligned binaries being closer to the limit $\mathbf{L}(r) \approx -\mathbf{S}(r)$ where transitional precession [51] occurs, violating assumptions (iii) and (iv) of Ref. [30].

All formulae are able to predict the angle $\vartheta_i(r_f)$ between the initial orbital angular momentum and the final spin with decent accuracy. The AEIn predictions are overall more accurate, but investigation of the angular dependence reveals that this accuracy deteriorates (as expected) when $q = 1/3$ and the spin of the larger black hole is nearly anti-aligned. In this limit the uncertainties increase up to $\sim 20^\circ$. This is again a consequence of those configurations approaching the transitional precession regime, where $\mathbf{L}(r) \approx -\mathbf{S}(r)$.

The AEIn prediction is unique in that it claims to predict $\vartheta_i(r_i)$ using the binary parameters at large separation without PN evolution. Our findings confirm (quite remarkably) that the majority of binaries in an initially isotropic ensemble result in a final spin which is nearly aligned with the orbital angular momentum at large binary separation. The values of θ_J shown in Figs. 10 and 11 suggest that this would not be the case for BBHs initially anti-aligned with \mathbf{L}_N . The accuracy of the AEIn

predictions also decreases for unequal masses (as expected and verified by our results for $q = 1/3$). More extreme mass ratios are expected to play a significant and possibly dominant role in the coalescence of SBH binaries [61–63], so it will be crucial to test the robustness of the Barausse-Rezzolla predictions for $q = 1/10$ and beyond. Accurate PN evolutions are more difficult in this regime, and we plan to investigate more extreme mass ratios in the future.

VII. DISCUSSION

In this paper, we examined how precession affects the distribution of spin orientations as BBHs inspiral from an initial separations $r_i \approx 1000M$ where gravitational radiation begins to dominate the dynamics, all the way down to separations $r_f \simeq 10M$ where numerical-relativity simulations typically begin.

We confirmed previous findings that isotropic spin distributions at $r_i \simeq 1000M$ remain isotropic at $r_f \simeq 10M$ [23, 26, 27]. However, torques exerted by circumbinary disks may partially align BBH spins with the orbital angular momentum at separations $r > r_i$ before gravitational radiation drives the inspiral [23]. Recent simulations suggest that the residual misalignment of the BBH spins with their accretion disk could typically be $\sim 10^\circ(30^\circ)$ for cold (hot) accretion disks, respectively [17]. Partially motivated by these findings, we carried out a more careful analysis of spin distributions that are partially aligned with the orbital angular momentum at $r = r_i$. We found that spin precession efficiently aligns the BBH spins with each other when the spin of the more massive black hole is initially partially aligned with the orbital angular momentum, increasing the final spin. We found the opposite trend when the spin of the more massive black hole is initially anti-aligned with the orbital angular momentum. Long evolutions are necessary to capture the full magnitude of the spin alignment. This could explain why these trends were not observed in the PN evolutions by Lousto *et al.* [27], which began at a fiducial binary separation $r = 50M$.

Some models of BBH evolution (see e.g. [61, 62]) suggest that SBH mergers might have comparable mass ratios ($q \lesssim 1$) at high redshift and more extreme mass ratios at low redshift. Since spin alignment is stronger for comparable-mass binaries, more alignment might be expected in SBH binaries at high redshifts. Observational arguments (see e.g. [64]) and magnetohydrodynamic simulations of accretion disks [65] provide some evidence that black hole spins are related to the radio loudness of quasars. If so, the inefficient alignment (and consequently smaller spins) produced by unequal-mass mergers at low redshift would at least be consistent with recent observational claims that the mean radiative efficiency of quasars decreases at low redshift [66, 67]. Stellar-mass black hole binaries should also have comparable mass ratios, so significant spin alignment could occur in such

systems as well.

We also pointed out that predictions of the final spin χ_f usually suffer from two sources of uncertainty: (i) the uncertainty in the *initial* frequency ω_i at which the BBH parameters are specified, and (ii) the uncertainty in the *final* separation r_f at which the given formula for χ_f should be applied. Both ambiguities are rooted in the rapid precessional modulation of the orbital parameters, which in turn results from the precessional timescale t_p being much shorter than the radiation timescale t_{GW} . Spin precession induces an intrinsic inaccuracy $\Delta\chi_f \lesssim 0.03$ in the dimensionless spin magnitude and $\Delta\vartheta_f \lesssim 20^\circ$ in the final spin direction.

The spin-orbit resonances studied in this paper should have significant effects on the distribution of gravitational recoil velocities resulting from BBH mergers, because the maximum recoil velocity has a strong dependence on spin alignment [15–17]. We plan to extend this study to investigate the predictions of different formulae for the recoil velocities that have been proposed in the literature.

Acknowledgements

We are particularly grateful to Vitor Cardoso for helping to test our numerical implementation of the PN evolution equations described in Sec. II, and to Étienne Racine for pointing out the possible relevance of the quadrupole-monopole interaction. We would also like to thank Enrico Barausse, Manuela Campanelli, Yanbei Chen, Pablo Laguna, Carlos Lousto, Samaya Nissanke, Evan Ochsner, Sterl Phinney and Manuel Tiglio for useful discussions. This work was supported by grants from the Sherman Fairchild Foundation to Caltech and by NSF grants No. PHY-0601459 (PI: Thorne) and PHY-090003 (TeraGrid). M.K. acknowledges support from NASA BEFS grant NNX07AH06G (PI: Phinney). E.B.’s research was supported by NSF grant PHY-0900735. U.S. acknowledges support from NSF grant PHY-0652995.

-
- [1] B. F. Schutz, *Nature* **323**, 310 (1986).
 - [2] D. E. Holz and S. A. Hughes, *Astrophys. J.* **629**, 15 (2005), astro-ph/0504616.
 - [3] M. C. Begelman, R. D. Blandford, and M. J. Rees, *Nature* **287**, 307 (1980).
 - [4] J. Frank and M. J. Rees, *Mon. Not. Roy. Astron. Soc.* **176**, 633 (1976).
 - [5] M. Milosavljevic and D. Merritt, *Astrophys. J.* **563**, 34 (2001), astro-ph/0103350.
 - [6] D. N. C. Lin and J. Papaloizou, *Mon. Not. Roy. Astron. Soc.* **188**, 191 (1979).
 - [7] P. Goldreich and S. Tremaine, *Astrophys. J.* **241**, 425 (1980).
 - [8] P. Chang, *Astrophys. J.* **684**, 236 (2008).
 - [9] P. C. Peters, *Phys. Rev.* **136**, B1224 (1964).
 - [10] A. Buonanno, Y. Chen, and T. Damour, *Phys. Rev.* **D74**, 104005 (2006), gr-qc/0508067.
 - [11] M. Campanelli, C. O. Lousto, H. Nakano, and Y. Zlochower, *Phys. Rev.* **D79**, 084010 (2009), 0808.0713.
 - [12] F. Pretorius, *Phys. Rev. Lett.* **95**, 121101 (2005), gr-qc/0507014.
 - [13] M. Campanelli, C. O. Lousto, P. Marronetti, and Y. Zlochower, *Phys. Rev. Lett.* **96**, 111101 (2006), gr-qc/0511048.
 - [14] J. G. Baker, J. Centrella, D.-I. Choi, M. Koppitz, and J. van Meter, *Phys. Rev. Lett.* **96**, 111102 (2006), gr-qc/0511103.
 - [15] J. A. Gonzalez, M. D. Hannam, U. Sperhake, B. Bruegmann, and S. Husa, *Phys. Rev. Lett.* **98**, 231101 (2007), gr-qc/0702052.
 - [16] M. Campanelli, C. O. Lousto, Y. Zlochower, and D. Merritt, *Astrophys. J.* **659**, L5 (2007), gr-qc/0701164.
 - [17] M. Dotti et al. (2009), 0910.5729.
 - [18] D. Merritt, M. Milosavljevic, M. Favata, S. A. Hughes, and D. E. Holz, *Astrophys. J.* **607**, L9 (2004), astro-ph/0402057.
 - [19] J. Magorrian et al., *Astron. J.* **115**, 2285 (1998), astro-ph/9708072.
 - [20] L. Ferrarese and D. Merritt, *Astrophys. J.* **539**, L9 (2000), astro-ph/0006053.
 - [21] S. Tremaine et al., *Astrophys. J.* **574**, 740 (2002), astro-ph/0203468.
 - [22] J. M. Bardeen and J. A. Petterson, *Astrophys. J.* **195**, L65 (1975).
 - [23] T. Bogdanovic, C. S. Reynolds, and M. C. Miller, *Astrophys. J.* **661**, L147 (2007), astro-ph/0703054.
 - [24] E. Berti and M. Volonteri, *Astrophys. J.* **684**, 822 (2008), 0802.0025.
 - [25] J. D. Schnittman, *Phys. Rev.* **D70**, 124020 (2004), astro-ph/0409174.
 - [26] F. Herrmann, J. Silberholz, M. Bellone, G. Guerberoff, and M. Tiglio (2009), 0908.3889.
 - [27] C. O. Lousto, H. Nakano, Y. Zlochower, and M. Campanelli (2009), 0910.3197.
 - [28] L. E. Kidder, *Phys. Rev.* **D52**, 821 (1995), gr-qc/9506022.
 - [29] A. Buonanno, Y.-b. Chen, and M. Vallisneri, *Phys. Rev.* **D67**, 104025 (2003), gr-qc/0211087.
 - [30] E. Barausse and L. Rezzolla, *Astrophys. J. Lett.* **704**, L40 (2009), 0904.2577.
 - [31] E. Barausse, E. Racine, and A. Buonanno, *Phys. Rev.* **D80**, 104025 (2009), 0907.4745.
 - [32] E. Barausse and A. Buonanno (2009), 0912.3517.
 - [33] E. Racine, *Phys. Rev.* **D78**, 044021 (2008), 0803.1820.
 - [34] E. Poisson, *Phys. Rev.* **D57**, 5287 (1998), gr-qc/9709032.
 - [35] B. Mikoczi, M. Vasuth, and L. A. Gergely, *Phys. Rev.* **D71**, 124043 (2005), astro-ph/0504538.
 - [36] E. Racine, A. Buonanno, and L. E. Kidder, *Phys. Rev.* **D80**, 044010 (2009), 0812.4413.
 - [37] W. H. Press, S. A. Teukolsky, W. T. Vetterling, and B. P. Flannery, *Numerical Recipes in C++ - The Art of Scientific Computing - Third Edition* (Cambridge University Press, 2007), ISBN 0-521-75033-4.
 - [38] L. Boyle, M. Kesden, and S. Nissanke, *Phys. Rev. Lett.* **100**, 151101 (2008), 0709.0299.
 - [39] L. Boyle and M. Kesden, *Phys. Rev.* **D78**, 024017 (2008),

- 0712.2819.
- [40] T. Damour, Phys. Rev. **D64**, 124013 (2001), gr-qc/0103018.
 - [41] A. Buonanno, G. B. Cook, and F. Pretorius, Phys. Rev. **D75**, 124018 (2007), gr-qc/0610122.
 - [42] E. Berti et al., Phys. Rev. **D76**, 064034 (2007), gr-qc/0703053.
 - [43] A. Buonanno et al., Phys. Rev. **D76**, 104049 (2007), 0706.3732.
 - [44] L. Rezzolla et al., Astrophys. **J679**, 1422 (2008), 0708.3999.
 - [45] L. Rezzolla et al., Astrophys. J. **674**, L29 (2008), 0710.3345.
 - [46] L. Rezzolla et al., Phys. Rev. **D78**, 044002 (2008), 0712.3541.
 - [47] W. Tichy and P. Marronetti, Phys. Rev. **D78**, 081501 (2008), 0807.2985.
 - [48] C. O. Lousto, M. Campanelli, and Y. Zlochower (2009), 0904.3541.
 - [49] A. Buonanno, L. E. Kidder, and L. Lehner, Phys. Rev. **D77**, 026004 (2008), 0709.3839.
 - [50] M. Kesden, Phys. Rev. **D78**, 084030 (2008), 0807.3043.
 - [51] T. A. Apostolatos, C. Cutler, G. J. Sussman, and K. S. Thorne, Phys. Rev. **D49**, 6274 (1994).
 - [52] M. Volonteri, F. Haardt, and P. Madau, Astrophys. J. **582**, 559 (2003), astro-ph/0207276.
 - [53] T. Tanaka and Z. Haiman, Astrophys. J. **696**, 1798 (2009), 0807.4702.
 - [54] C. d. P. Lagos, N. D. Padilla, and S. A. Cora (2009), 0901.0547.
 - [55] D. Sijacki, V. Springel, and M. G. Haehnelt (2009), 0905.1689.
 - [56] N. Fanidakis et al. (2009), 0911.1128.
 - [57] M. Dotti, R. Salvaterra, A. Sesana, M. Colpi, and F. Haardt, Mon. Not. Roy. Astron. Soc. **372**, 869 (2006), astro-ph/0605624.
 - [58] Z. Lippai, Z. Frei, and Z. Haiman (2008), 0801.0739.
 - [59] J. D. Schnittman and J. H. Krolik (2008), 0802.3556.
 - [60] G. A. Shields and E. W. Bonning (2008), 0802.3873.
 - [61] S. M. Koushiappas and A. R. Zentner, Astrophys. J. **639**, 7 (2006), astro-ph/0503511.
 - [62] A. Sesana, M. Volonteri, and F. Haardt, Mon. Not. Roy. Astron. Soc. **377**, 1711 (2007), astro-ph/0701556.
 - [63] L. A. Gergely and P. L. Biermann, Astrophys. J. **697**, 1621 (2009), 0704.1968.
 - [64] M. Volonteri, M. Sikora, and J.-P. Lasota (2007), 0706.3900.
 - [65] A. Tchekhovskoy, R. Narayan, and J. C. McKinney (2009), 0911.2228.
 - [66] J. M. Wang et al., Astrophys. J. **697**, L141 (2009), 0904.1896.
 - [67] Y.-R. Li, J.-M. Wang, Y.-F. Yuan, and S. Zhang, Astrophys. J. **710**, 878 (2010), 1001.5170.

TABLE I: Mean and standard deviation of the final spin magnitudes predicted for different sets of maximally spinning BBH mergers. The first column lists the formulae used to predict the final spins, as described in Sec. V. The second column gives the mass ratio q . Each set of BBHs begins at $r_i = 1000M$ with the indicated value of θ_1 and flat distributions of $\cos\theta_2$ and $\Delta\phi$. The third, fourth, and fifth columns show the mean and deviation expected if the BBH spins do not precess, thus maintaining their initial distributions at $r_i = 1000M$ until merger. The sixth, seventh, and eighth columns assume that the spins precess according to the PN equations of Sec. II as they inspiral to $r_f = 10M$, at which separation we apply the spin formulae.

model	q	$r_i = 1000M$			$r_f = 10M$		
		$\theta_1 = 10^\circ$	$\theta_1 = 20^\circ$	$\theta_1 = 30^\circ$	$\theta_1 = 10^\circ$	$\theta_1 = 20^\circ$	$\theta_1 = 30^\circ$
AEIn	9/11	0.867 ± 0.064	0.863 ± 0.065	0.857 ± 0.066	0.914 ± 0.034	0.905 ± 0.036	0.892 ± 0.038
AEIo	9/11	0.866 ± 0.063	0.863 ± 0.064	0.856 ± 0.065	0.912 ± 0.034	0.904 ± 0.036	0.891 ± 0.038
FAU	9/11	0.873 ± 0.059	0.868 ± 0.060	0.861 ± 0.061	0.909 ± 0.035	0.901 ± 0.037	0.888 ± 0.039
BKL	9/11	0.862 ± 0.067	0.858 ± 0.068	0.851 ± 0.070	0.905 ± 0.037	0.898 ± 0.039	0.884 ± 0.042
Kes	9/11	0.901 ± 0.072	0.896 ± 0.073	0.889 ± 0.075	0.950 ± 0.038	0.941 ± 0.041	0.927 ± 0.044
AEIn	2/3	0.886 ± 0.052	0.882 ± 0.053	0.875 ± 0.054	0.922 ± 0.030	0.914 ± 0.031	0.900 ± 0.034
AEIo	2/3	0.886 ± 0.052	0.882 ± 0.052	0.876 ± 0.054	0.922 ± 0.030	0.914 ± 0.031	0.900 ± 0.034
FAU	2/3	0.901 ± 0.043	0.895 ± 0.044	0.886 ± 0.046	0.924 ± 0.029	0.915 ± 0.030	0.901 ± 0.031
BKL	2/3	0.882 ± 0.052	0.878 ± 0.053	0.870 ± 0.054	0.914 ± 0.031	0.906 ± 0.032	0.893 ± 0.035
Kes	2/3	0.921 ± 0.056	0.917 ± 0.057	0.909 ± 0.059	0.958 ± 0.031	0.949 ± 0.034	0.935 ± 0.037
AEIn	1/3	0.950 ± 0.025	0.946 ± 0.025	0.938 ± 0.026	0.957 ± 0.023	0.951 ± 0.023	0.941 ± 0.022
AEIo	1/3	0.958 ± 0.025	0.953 ± 0.026	0.944 ± 0.026	0.964 ± 0.023	0.958 ± 0.023	0.947 ± 0.022
FAU	1/3	0.972 ± 0.013	0.964 ± 0.014	0.951 ± 0.016	0.975 ± 0.012	0.966 ± 0.012	0.953 ± 0.011
BKL	1/3	0.931 ± 0.020	0.927 ± 0.020	0.921 ± 0.021	0.936 ± 0.018	0.931 ± 0.018	0.923 ± 0.018
Kes	1/3	0.968 ± 0.021	0.965 ± 0.022	0.958 ± 0.023	0.974 ± 0.019	0.970 ± 0.019	0.962 ± 0.020
model	q	$\theta_1 = 150^\circ$	$\theta_1 = 160^\circ$	$\theta_1 = 170^\circ$	$\theta_1 = 150^\circ$	$\theta_1 = 160^\circ$	$\theta_1 = 170^\circ$
AEIn	9/11	0.551 ± 0.080	0.527 ± 0.080	0.511 ± 0.079	0.535 ± 0.072	0.510 ± 0.076	0.493 ± 0.080
AEIo	9/11	0.551 ± 0.080	0.527 ± 0.080	0.512 ± 0.079	0.535 ± 0.072	0.510 ± 0.077	0.493 ± 0.080
FAU	9/11	0.542 ± 0.076	0.520 ± 0.076	0.506 ± 0.076	0.530 ± 0.070	0.507 ± 0.074	0.492 ± 0.076
BKL	9/11	0.514 ± 0.088	0.488 ± 0.087	0.471 ± 0.086	0.496 ± 0.078	0.468 ± 0.083	0.449 ± 0.087
Kes	9/11	0.531 ± 0.091	0.504 ± 0.090	0.486 ± 0.089	0.512 ± 0.081	0.483 ± 0.087	0.463 ± 0.091
AEIn	2/3	0.500 ± 0.067	0.467 ± 0.066	0.445 ± 0.065	0.490 ± 0.057	0.456 ± 0.062	0.432 ± 0.065
AEIo	2/3	0.499 ± 0.067	0.466 ± 0.067	0.444 ± 0.066	0.489 ± 0.057	0.455 ± 0.062	0.432 ± 0.065
FAU	2/3	0.490 ± 0.060	0.460 ± 0.060	0.441 ± 0.059	0.483 ± 0.053	0.452 ± 0.056	0.432 ± 0.059
BKL	2/3	0.465 ± 0.072	0.430 ± 0.071	0.405 ± 0.070	0.454 ± 0.060	0.416 ± 0.066	0.390 ± 0.070
Kes	2/3	0.480 ± 0.075	0.442 ± 0.071	0.417 ± 0.072	0.468 ± 0.063	0.428 ± 0.068	0.401 ± 0.072
AEIn	1/3	0.324 ± 0.034	0.233 ± 0.034	0.151 ± 0.032	0.323 ± 0.013	0.231 ± 0.015	0.145 ± 0.021
AEIo	1/3	0.321 ± 0.034	0.230 ± 0.034	0.146 ± 0.032	0.319 ± 0.012	0.227 ± 0.015	0.140 ± 0.021
FAU	1/3	0.301 ± 0.026	0.222 ± 0.026	0.154 ± 0.024	0.300 ± 0.016	0.220 ± 0.018	0.151 ± 0.020
BKL	1/3	0.315 ± 0.034	0.222 ± 0.034	0.136 ± 0.032	0.313 ± 0.011	0.219 ± 0.013	0.130 ± 0.019
Kes	1/3	0.322 ± 0.035	0.227 ± 0.035	0.139 ± 0.033	0.320 ± 0.012	0.224 ± 0.014	0.133 ± 0.019

TABLE II: Uncertainty distributions in χ_f and in the various angles describing the final spin directions, as predicted by the formulae listed in Sec. V. The uncertainties and their standard deviations are obtained by evolving uniform $10 \times 10 \times 10$ grids of maximally spinning BBHs with mass ratio $q = 9/11$, $2/3$ and $1/3$, respectively.

model	q	$\Delta\chi_f(r = 10M)$	$\Delta\vartheta_f(r = 10M)$	$\Delta\vartheta_i(r = 10M)$	$\Delta\vartheta_i(r = 1000M)$
AEIn	9/11	0.0159 ± 0.0099	8.38 ± 5.30	1.47 ± 1.09	1.48 ± 1.10
AEIo	9/11	0.0155 ± 0.0098	11.38 ± 6.18	6.55 ± 2.73	—
FAU	9/11	0.0021 ± 0.0035	8.51 ± 4.75	3.67 ± 1.68	—
BKL	9/11	0.0153 ± 0.0094	11.74 ± 6.39	6.89 ± 2.92	—
Kes	9/11	0.0174 ± 0.0105	11.99 ± 6.51	7.04 ± 2.96	—
AEIn	2/3	0.0205 ± 0.0127	11.96 ± 6.17	1.81 ± 1.21	1.83 ± 1.24
AEIo	2/3	0.0199 ± 0.0124	14.10 ± 6.99	7.37 ± 2.80	—
FAU	2/3	0.0034 ± 0.0026	10.66 ± 5.61	4.41 ± 1.76	—
BKL	2/3	0.0191 ± 0.0108	14.52 ± 7.05	7.79 ± 2.98	—
Kes	2/3	0.0217 ± 0.0124	14.83 ± 7.24	8.02 ± 2.99	—
AEIn	1/3	0.0165 ± 0.0109	8.58 ± 4.17	3.96 ± 4.46	4.25 ± 5.16
AEIo	1/3	0.0156 ± 0.0101	9.57 ± 4.62	10.45 ± 4.12	—
FAU	1/3	0.0177 ± 0.0090	7.80 ± 3.84	6.60 ± 2.75	—
BKL	1/3	0.0148 ± 0.0089	9.81 ± 4.79	11.24 ± 4.45	—
Kes	1/3	0.0167 ± 0.0105	10.01 ± 5.06	11.49 ± 4.48	—